HAL open science

Non-LTE time-dependent spectroscopic modelling of Type II-plateau supernovae from the photospheric to the nebular phase: case study for 15 and 25 M-circle dot progenitor stars

Luc Dessart, D. John Hillier

▶ **To cite this version:**

Luc Dessart, D. John Hillier. Non-LTE time-dependent spectroscopic modelling of Type II-plateau supernovae from the photospheric to the nebular phase: case study for 15 and 25 M-circle dot progenitor stars. Monthly Notices of the Royal Astronomical Society, 2011, 410 (3), pp.1739–1760. 10.1111/j.1365-2966.2010.17557.x . hal-01438874

HAL Id: hal-01438874

https://hal.science/hal-01438874v1

Submitted on 30 Nov 2021

HAL is a multi-disciplinary open access archive for the deposit and dissemination of scientific research documents, whether they are published or not. The documents may come from teaching and research institutions in France or abroad, or from public or private research centers.

L'archive ouverte pluridisciplinaire **HAL**, est destinée au dépôt et à la diffusion de documents scientifiques de niveau recherche, publiés ou non, émanant des établissements d'enseignement et de recherche français ou étrangers, des laboratoires publics ou privés.

Distributed under a Creative Commons Attribution 4.0 International License

Monthly Notices of the ROYAL ASTRONOMICAL SOCIETY

Mon. Not. R. Astron. Soc. **410,** 1739–1760 (2011) doi:10.1111/j.1365-2966.2010.17557.x

Non-LTE time-dependent spectroscopic modelling of Type II-plateau supernovae from the photospheric to the nebular phase: case study for 15 and 25 $M_\odot$ progenitor stars

Luc Dessart[1★] and D. John Hillier[2]

[1]*Laboratoire d'Astrophysique de Marseille, Université de Provence, CNRS, 38 rue Frédéric Joliot-Curie, F-13388 Marseille Cedex 13, France*
[2]*Department of Physics and Astronomy, University of Pittsburgh, 3941 O'Hara Street, Pittsburgh, PA 15260, USA*

Accepted 2010 August 17. Received 2010 August 13; in original form 2010 July 5

ABSTRACT

We present the first non-LTE time-dependent radiative-transfer simulations of supernovae (SNe) II-Plateau (II-P) covering both the photospheric and nebular phases, from ∼10 to $\gtrsim$1000 d after the explosion, and based on 1.2 B piston-driven ejecta produced from a 15 $M_\odot$ and a 25 $M_\odot$ non-rotating solar-metallicity star. The radial expansion of the gradually cooling photosphere gives rise to a near-constant luminosity up to $\gtrsim$100 d after the explosion. The photosphere remains in the outer 0.5 $M_\odot$ of the ejecta for up to ∼50 d after the explosion. As the photosphere reaches the edge of the helium core, the SN luminosity drops by an amount mitigated by the progenitor radius and the ^{56}Ni mass. Synthetic light curves exhibit a bell-shaped morphology, evolving faster for more compact progenitors, and with an earlier peak and narrower width in bluer filters. UV and *U*-band fluxes are very sensitive to line blanketing, the metallicity and the adopted model atoms. During the recombination epoch synthetic spectra are dominated by H I and metal lines, and are largely insensitive to the differing H/He/C/N/O composition of our two progenitor stars. In contrast, synthetic nebular-phase spectra reveal a broader/stronger O I doublet line in the higher-mass progenitor model, reflecting the larger masses of oxygen and nickel that are ejected. Our simulations overestimate the typical luminosity and the visual rise time of standard SNe II-P, most likely a consequence of our progenitor stars being too big and/or too hydrogen rich. Comparison of our simulations with photospheric-phase observations of SN1999em of the same colour is satisfactory. Our neglect of non-thermal excitation/ionization leads to a fast disappearance of continuum radiation and Balmer-line emission at the end of the plateau phase. With the exception of H I lines, our nebular spectra show a striking similarity to contemporaneous observations of SN1999em.

Key words: radiative transfer – stars: atmospheres – supernovae: individual: SN1999em – supernovae: individual: SN1987A.

1 INTRODUCTION

Supernovae (SNe) II-Plateau (II-P) are the most represented SN type (Cappellaro et al. 1997; Smartt et al. 2009). The theoretical prediction that they stem from the explosion of red-supergiant (RSG) stars (Colgate & White 1966; Falk & Arnett 1977) is supported by direct identification of some SNe II-Ps with their progenitor on pre-explosion images. The progenitors indicate main-sequence masses in the range 8–17 $M_\odot$ (see Smartt 2009 for a review). After their death, SN II-P produce a stellar-mass compact object, either a neutron star or a black hole (Heger et al. 2003). They are a key driver for the chemical evolution of galaxies through the core-embedded material they eject (in particular oxygen; Woosley & Weaver 1995), as well as efficient dust factories (Sugerman et al. 2006).

Owing to their large luminosity, SNe II-P offer a means to constrain distances in the Universe through a variety of methods known as the Expanding Photosphere Method (Kirshner & Kwan 1974; Eastman, Schmidt & Kirshner 1996; Dessart & Hillier 2005a, 2006), the Spectral-fitting Expanding Atmosphere Method (Mitchell et al. 2002) and the Standard Candle Method (Hamuy & Pinto 2002). Studying SNe II-P is thus of relevance for a wide range of topics in modern astrophysics.

Inferences on SNe II-P ejecta, as well as their progenitor stars, can be made using radiation hydrodynamics and radiative transfer. For multi-band light-curve calculations, radiation hydrodynamics assuming the gas in Local Thermodynamic Equilibrium (LTE), frequency-mean or frequency-dependent opacities (including lines

★E-mail: luc.dessart@oamp.fr

© 2010 The Authors
Monthly Notices of the Royal Astronomical Society © 2010 RAS

Downloaded from https://academic.oup.com/mnras/article/410/3/1739/962985 by CNRS - ISTO user on 30 November 2021

or not) and time-dependent radiation transport are used with some success to constrain the explosion energy, the mass of the ejecta, the radius of the progenitor star and the amount of ^{56}Ni produced in the explosion (e.g. Falk & Arnett 1977; Litvinova & Nadezhin 1985; Blinnikov et al. 2000; Baklanov, Blinnikov & Pavlyuk 2005; Utrobin 2007; Tominaga et al. 2009; Dessart, Livne & Waldman 2010a,b). Calibrations drawn from such studies have been used to infer SNe II-P properties (Hamuy 2003).

However, an attractive and more physically consistent alternative is to use radiation hydrodynamics up to a few days after shock-breakout, when acceleration terms are sizeable, and then switch to a more sophisticated radiative-transfer treatment on a non-accelerating ejecta (Eastman et al. 1994; Kasen & Woosley 2009; Dessart & Hillier 2010). This then permits a more detailed treatment of line blanketing, departures from LTE and the dependence of the radiation field on frequency, angle and time. Recently, we sketched an approach that treats all these important aspects (Dessart & Hillier 2010) and applied it to the early evolution of SN1987A. The method retains the sophistication of non-LTE steady-state simulations focusing on the decoupling layers of SN ejecta (Dessart & Hillier 2005b; Baron, Branch & Hauschildt 2007; Dessart et al. 2008), but also treats important time-dependent terms appearing in the energy, statistical-equilibrium and radiative-transfer equations (see e.g. Utrobin & Chugai 2005; Dessart & Hillier 2008, for a partial treatment of these terms).

This initial-value problem is constrained at the start by employing a hydrodynamical input model of the explosion, itself generated from a physically consistent pre-SN model. Confrontation of synthetic spectra and light curves with observations can thus be connected to the known ejecta properties, yielding constraints on the explosion and the progenitor properties. Because we explicitly treat all processes controlling level populations, the effects of line emission, absorption and overlap are accurately computed, and thus line profiles can be used to extract information on the ejecta. Accurate spectral modelling is critical for the determination of abundances, excitation/ionization sources, kinematics, and ultimately the explosion and progenitor properties. By contrast, most SN studies treat bound–bound transitions approximately. These studies allow inferences based on colour and light-curve evolution but little reliable information is extracted from lines.

In this paper, building upon our recent analysis of the Type II-peculiar SN1987A (Dessart & Hillier 2010), we present the first non-LTE time-dependent radiative-transfer simulations of SNe II-P using CMFGEN (Hillier & Miller 1998; Dessart & Hillier 2005b, 2008), covering both the photospheric and nebular phases. Because of the huge computational expense of this endeavour, we focus on only two ejecta produced from the explosion of stars with main-sequence masses of 15 and 25 $M_\odot$, and characterized by an explosion energy of 1.2 B (Woosley, private communication; Woosley & Heger 2007). We use these simulations to describe fundamental properties of the SN gas and light, with special emphasis on spectra which have not previously been computed with this level of physical consistency in this context. Due to the limited set of inputs, we make no attempt to reproduce specific observations, but rather we seek to make a qualitative assessment of the general adequacy of our models.

In the next section, we present the pre-SN models that were used to generate the hydrodynamical input ejecta from which our radiative-transfer simulations start. The adopted model atoms, atomic data and the importance of non-LTE are discussed in Section 3. In Section 4, we discuss the evolution of the gas properties throughout the photospheric and nebular phases, including the photospheric properties and the ejecta ionization. We then turn to our theoretical results for the radiation field. In Section 5, we first describe the bolometric-light evolution and multi-band light curves, before moving on to synthetic spectra, the sources of blanketing and line identifications in Section 6. We also document the spectral differences predicted in our simulations for the low and the high-mass progenitor models. In Section 7, we compare our results to photometric and spectroscopic observations of SNe II-P in general, and of SN1999em in particular, to identify the successes and failures of our simulations. In Section 8, we present our conclusions and plans for a forthcoming parameter study of SNe II-P.

2 INITIAL HYDRODYNAMICAL MODEL AND SETUP

The approach we follow is similar to that described in Dessart & Hillier (2010), but we now concentrate on the SN ejecta resulting from the explosion of RSG stars. Starting from a hydrodynamical model that describes the depth variation of element mass fraction, density, temperature, radius and velocity, we model the non-LTE time-dependent radiative transfer of SNe II-P ejecta with CMFGEN (Hillier & Miller 1998; Dessart & Hillier 2005b, 2008, 2010). We assume the SN is spherically symmetric and smooth (i.e. un-clumped), and free from external disturbances, such as interaction with the circumstellar environment or irradiation from the newly born neutron star. The hydrodynamical models were computed by Woosley & Heger (2007) using the code KEPLER (Weaver, Zimmerman & Woosley 1978) by first evolving non-rotating, solar-metallicity, 15 $M_\odot$ and 25 $M_\odot$ stars from the main sequence to the formation and collapse of their degenerate iron core, and then exploding these by means of a piston.

The input model s15e12 (s25e12) was generated from model s15A (s25) of Woosley & Heger (2007) and corresponds to an SN ejecta with a 1.2 B energy and post-explosion time of 8×10^5 s (2×10^6 s; see Table 1 for details). For the same ejecta kinetic energy, the model s25e12 yields a higher mass of ^{56}Ni (0.163 compared to 0.0866 $M_\odot$) because it possesses a larger helium-core mass with more mass at larger density, smaller radii and higher temperatures. All models were artificially mixed by sweeping a 'box' four times through the ejecta and averaging the composition within that box. The box used in model s15e12 (s25e12) had a width of 0.427 $M_\odot$ (0.819 $M_\odot$), corresponding in each case to a tenth of the progenitor helium-core mass. This moderate mixing softens the composition gradients but preserves the strong ejecta stratification, hydrogen being absent in the inner few solar masses of the ejecta (below 1500 km s^{-1}). The ^{56}Ni mass fraction is sizeable only below 1000–2000 km s^{-1} but owing to mixing shows a non-zero mass fraction even at the outer edge of the ejecta.

In the (standard) KEPLER models s15e12 and s25e12, the species included are H, ^{3}He, ^{4}He, ^{12}C, ^{14}N, ^{16}O, ^{20}O, ^{24}Mg, ^{28}Si, ^{32}S, ^{36}Ar, ^{40}Ca, ^{44}Ti, ^{48}Cr, ^{52}Fe, ^{54}Fe, ^{56}Ni, ^{56}Fe and 'Fe'. In this nomenclature, some species approximate certain nuclei. For example, ^{4}He

Table 1. Properties of the pre-SN models s15 and s25 (Woosley & Heger 2007). The age is the time elapsed between the main sequence and core collapse.

Model	M_i ($M_\odot$)	M_f ($M_\odot$)	$R_\star$ ($R_\odot$)	Age (Myr)	M_{ejecta} ($M_\odot$)	$M_{remnant}$ ($M_\odot$)
s15	15	12.79	810	13.24	10.93	1.83
s25	25	15.84	1350	7.47	13.94	1.90

Downloaded from https://academic.oup.com/mnras/article/410/3/1739/962985 by CNRS - ISTO user on 30 November 2021

Table 2. Ejecta cumulative yields (upper table) and surface mass fraction (lower table) for the most abundant species in models s15e12 and s25e12. Metal abundances not shown here are taken at the solar-metallicity value. The total ejecta mass is 10.93 $M_\odot$ (13.94 $M_\odot$) for model s15e12 (s25e12). Model s15e12iso has the same ejecta characteristics as model s15e12 and differs only in composition of underabundant species, e.g. Sc or Ba. Numbers in parentheses correspond to powers of 10.

Model	Ejecta cumulative yields														
	M_H ($M_\odot$)	M_{He} ($M_\odot$)	M_C ($M_\odot$)	M_N ($M_\odot$)	M_O ($M_\odot$)	M_{Ne} ($M_\odot$)	M_{Mg} ($M_\odot$)	M_{Si} ($M_\odot$)	M_S ($M_\odot$)	M_{Ar} ($M_\odot$)	M_{Ca} ($M_\odot$)	M_{Ti} ($M_\odot$)	M_{Cr} ($M_\odot$)	M_{Fe} ($M_\odot$)	$M_{^{56}Ni}$ ($M_\odot$)
s15e12	5.49(0)	4.00(0)	1.59(-1)	3.22(-2)	8.16(-1)	1.52(-1)	5.41(-2)	8.10(-2)	3.17(-2)	6.43(-3)	5.52(-3)	1.26(-4)	1.29(-3)	1.60(-2)	8.66(-2)
s25e12	4.01(0)	4.77(0)	3.53(-1)	4.48(-2)	3.32(0)	5.30(-1)	2.24(-1)	3.16(-1)	1.49(-1)	2.58(-2)	1.85(-2)	1.54(-4)	2.48(-3)	2.04(-2)	1.63(-1)
Model	Ejecta surface mass fractions														
	X_H	X_{He}	X_C	X_N	X_O	X_{Ne}	X_{Mg}	X_{Si}	X_S	X_{Ar}	X_{Ca}	X_{Ti}	X_{Cr}	X_{Fe}	$X_{^{56}Ni}$
s15e12	6.50(-1)	3.35(-1)	1.42(-3)	3.11(-3)	5.41(-3)	1.31(-3)	7.91(-4)	8.29(-4)	4.23(-4)	1.13(-4)	7.38(-5)	3.83(-6)	3.43(-5)	1.46(-3)	1.14(-9)
s25e12	5.28(-1)	4.56(-1)	9.17(-4)	5.54(-3)	3.89(-3)	1.37(-3)	8.03(-4)	8.33(-4)	4.25(-4)	1.13(-4)	7.40(-5)	3.83(-6)	3.43(-5)	1.46(-3)	1.58(-6)

approximates nuclei with $1 < A < 6$, where A is the atomic mass, and ^{48}Cr stands for nuclei with $47 < A < 52$ [see Woosley, Heger & Weaver (2002) for details]. In such inputs, numerous species are not described individually (e.g. Na, although Na I lines are unambiguously seen in SNe II-P spectra and require the knowledge of the sodium abundance for a proper modelling). Some, like Ba, are altogether ignored. We give a summary of the chemical composition for the dominant species in Table 2, with both the cumulative ejecta yields (upper table) and the corresponding mass fractions at the progenitor surface (lower table). We also illustrate the distribution of the main elements through the ejecta in Fig. 1. Surface abundances of both models show evidence for CNO processing, with the higher-mass model exhibiting larger enhancements of both He and N, and a greater depletion of C and O. The presence of CNO processed material in RSG atmospheres is corroborated by spectroscopic analyses of RSG stars (Lançon et al. 2007), and understood to stem, in the absence of rotation, from convective dredge-up. Stellar rotation is expected to aid the appearance of CNO processed material at the stellar surface (Meynet & Maeder 2000; Meynet, Ekström & Maeder 2006). In the outer regions of the ejecta, mass fractions for elements heavier than oxygen are identical for both models and correspond to the solar metallicity (apart from the nucleosynthesized ^{56}Ni).

The bulk of the kinetic energy is contained within the hydrogen-rich regions of the ejecta, while the region corresponding to the helium core contains $\lesssim$10 per cent of the total kinetic energy in model s25e12, and an even lower fraction in the model s15e12 (see top axis in Fig. 1). The higher mass progenitor (which suffered enhanced mass loss) has a lower mass hydrogen-rich envelope and a larger helium/oxygen ejected mass (Fig. 1). As we discuss in this paper in relation to the degeneracy of photospheric-phase SNe II-P spectra and light curves, the enhanced mass of ejected oxygen may be most easily identified in SNe II-P observations taken at nebular times. Because it pertains to the systematic increase in helium-core mass with main sequence, it can help constrain the progenitor identity (Dessart et al. 2010a).

In parallel to the simulation based on model s15e12, we also perform a CMFGEN simulation based on the detailed KEPLER model

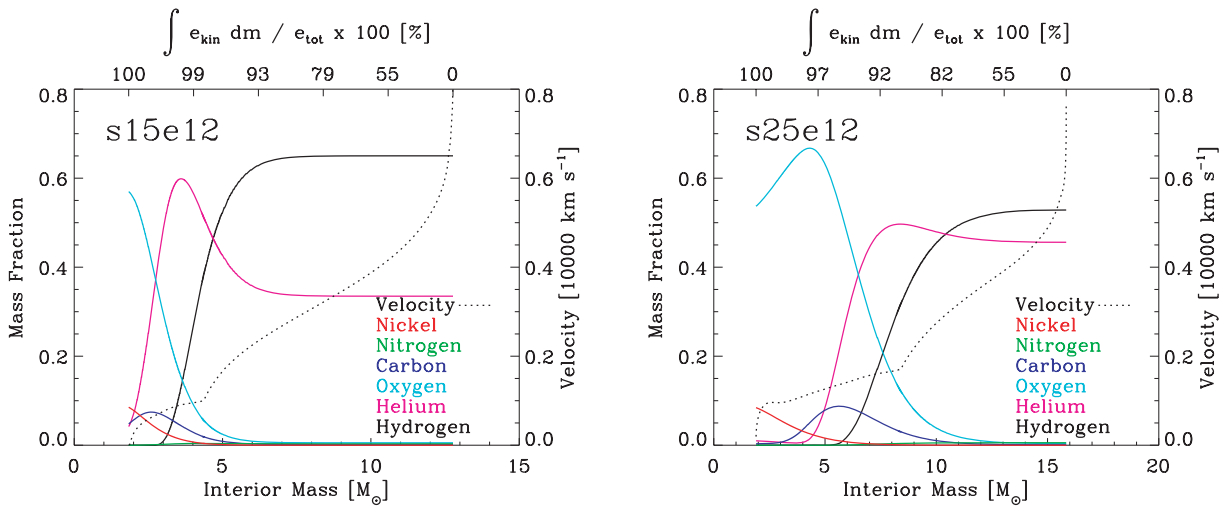

Figure 1. Left: element mass fractions as a function of Lagrangian mass for the hydrodynamical input model s15e12. We show hydrogen (black), helium (pink), oxygen (turquoise), carbon (blue), nitrogen (green) and ^{56}Ni (red). We also overplot the velocity as a dotted black line, with the corresponding axis given on the right. We include an axis at the top showing the distribution of the mass-integrated specific kinetic energy (the integral bounds being the Lagrangian mass M_r and M_{tot}). The bulk of the ejecta kinetic energy is contained within what used to be the loosely bound hydrogen-rich region of the progenitor envelope. In contrast, the more gravitationally bound helium core is ultimately endowed with only a few per cent of the total ejecta kinetic energy. Right: same as left, but now for the s25e12 model. The helium core is endowed with a larger fraction of the total ejecta kinetic energy than seen in the s15e12 model, although the largest share is still contained in the hydrogen-rich region of the ejecta. For both models, the total ejecta kinetic energy is 1.2 B.

© 2010 The Authors, MNRAS **410,** 1739–1760
Monthly Notices of the Royal Astronomical Society © 2010 RAS

Downloaded from https://academic.oup.com/mnras/article/410/3/1739/962985 by CNRS - ISTO user on 30 November 2021

s15e12iso, which has exactly the same structure in density/radius/velocity/temperature, but was evolved with a more complete nuclear network. The KEPLER model s15e12iso includes every element of the periodic table (as well as all its associated isotopes) up to Astatine (symbol At; $Z = 85$). This detailed input permits the specific modelling of any species (and associated ions). In practice, apart from unstable isotopes, we use the sum of the individual isotopic mass fractions to determine the abundance of the associated species. Compared to models s15e12 and s25e12, our simulation of model s15e12iso treats in addition the elements Ne, Na (no longer assumed to have an abundance at the solar-metallicity value and constant with depth), Al, Ar, Ti, Sc, Cr and Ba, adopting the abundance distributions computed by KEPLER. With this choice, we include all species that have a mass fraction larger than $\sim 10^{-5}$ at any depth in the s15e12iso ejecta, as well as any species with identified features in SNe II-P spectra (e.g. Sc and Ba). When discussing general ejecta and radiation properties, we employ our simulations based on the s15e12 and s25e12 models, but when comparing to observations we employ our simulations based on model s15e12iso as it describes more completely the ejecta composition and the effects of line blanketing.

Before starting our radiative-transfer calculations, we made a number of adjustments to the hydrodynamical inputs. In both models, the innermost regions are not in homologous expansion (despite the ejecta age of 9.26 and 23.15 d for models s15e12 and s25e12, respectively) so we enforce $r/v =$ constant (adopting a mid-point in the ejecta) for compatibility with the radiative-transfer algorithm which assumes $\mathrm{d}v/\mathrm{d}r = v/r$. This artificially enhances the small velocity of the inner regions by $\lesssim$50 per cent in model s15e12 and by $\sim$10 per cent in model s25e12. To ensure the radiation is free streaming at all wavelengths at the outer boundary, and to correct for the poorly resolved outer region in the input model, we trim and stitch an outer region to the input model (characterized by a power-law density with an exponent of 15), extending it to larger radii/velocities. The photosphere is always located interior to this outer region, and is thus not directly affected by this manipulation (see Section 4). At the new outer boundary, densities are on the order of 10^{-20} g cm^{-3} and velocities on the order of 20 000 km s^{-1}. To illustrate these adjustments, we show in Fig. 2 the ejecta properties provided by KEPLER and those we start with in our CMFGEN simulations.

One issue of concern is the starting conditions. In our approach we fix the temperature to that of the hydrodynamical simulation and solve the relativistic transfer equation and statistical equilibrium equations neglecting time-dependent effects. For the models presented here this is likely to be a reasonable approximation. Steady-state CMFGEN models showed that time-dependent effects for SN1999em did not become noticeable in spectra until day 16 (Dessart & Hillier 2006). On the other hand, our starting times would be unreasonable for SN1987A, where time-dependent effects are already important at day 4 (Utrobin & Chugai 2005; Dessart & Hillier 2010). The reasons for starting these exploratory simulations late were two fold – the need to run many additional models at earlier time-steps was considered unnecessarily wasteful, and the assumption of a homologous expansion at earlier times is increasingly problematic.

The post-explosion time corresponding to our 'adjusted' inputs has been modified by 5-8 per cent (because of the enforcement of homology) so the ejecta age is 8.51 d (22.01 d) for our initial simulation based on model s15e12 (s25e12). To step in time, we adopt a fixed logarithmic increment, $\Delta t/t \sim 0.1$ and continue the simulations just past 1000 d (we also run simulations using a fixed 2-d time increment to cover the rapid fading at the end of the plateau phase). For the simulation based on model s15e12 (s25e12), the sequence covers until 1040 d (1037 d) in 52 (43) steps and took about 3 months to complete for each. As in Dessart & Hillier (2010)

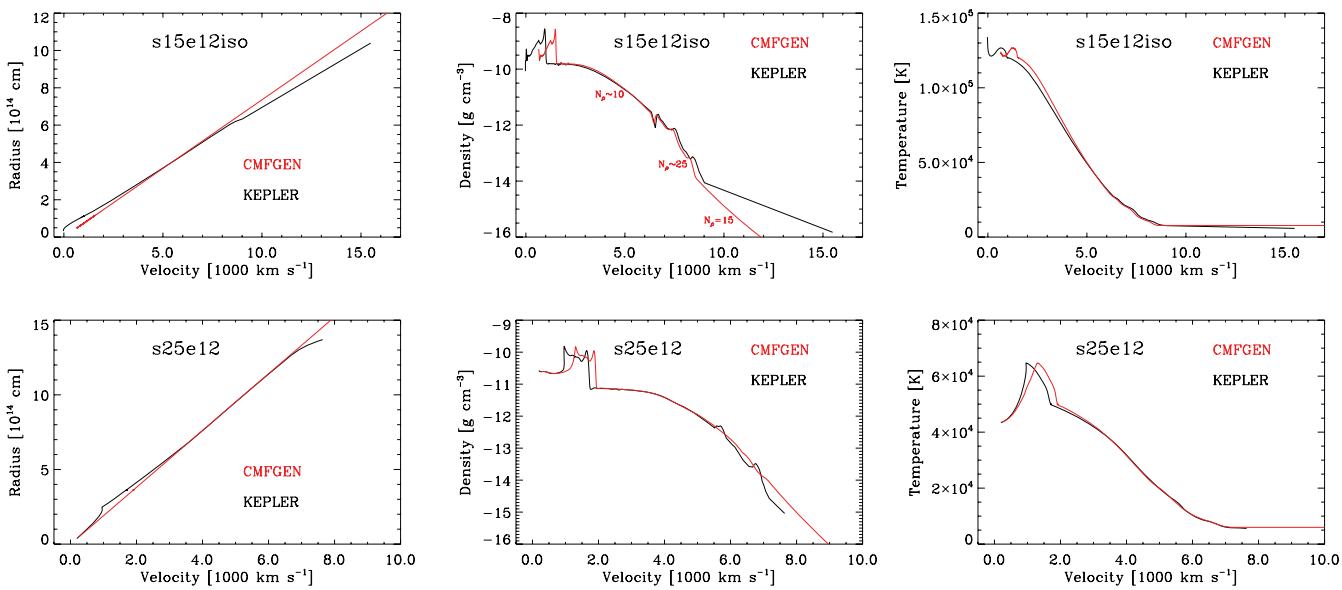

Figure 2. Top row: comparison between the initial KEPLER hydrodynamical input s15e12iso (black) and the corresponding ejecta structure we start with for the radiative-transfer simulations (red). The differences between the two arise from our need of strict-homologous expansion ($r/v =$ constant) and of an outer optically thin region where photons are freely streaming (which requires we stitch this outer region, which is lacking, to the KEPLER model). In the process, we artificially speed up regions with $v < 2000$ km s^{-1} by $\lesssim$50 per cent and smooth the density structure of the SN ejecta. We indicate in the middle panel the density exponent $N_\rho = -d \log \rho / d \log v$ for the inner, intermediate and outer ejecta regions. As discussed in Section 4, the photosphere resides in the region of steep density decline with $N_\rho \sim 20 - 25$ and $7.5 < V_{\rm phot}/(1000\,{\rm km\,s^{-1}}) < 9$ for up to three weeks after explosion in model s15e12iso. Bottom row: same as top row, but now for model s25e12. The speed-up of the inner regions is smaller, approximately 10 per cent, because we start with a model that is closer to homologous expansion.

Downloaded from https://academic.oup.com/mnras/article/410/3/1739/962985 by CNRS - ISTO user on 30 November 2021

the gas temperature is held fixed, and set to that provided by the hydrodynamical input model, for the first model in the sequence. For subsequent models, the temperature is solved for everywhere. Hence, only results from the second time-step and onwards are shown or discussed here (corresponding to ages 9.3 and 24.0 d for simulations based on models s15e12 and s25e12). We impose a floor value to the gas temperature to avoid problems with the evaluation of exponentials involving high ionization stages. Since the ejecta cool as time proceeds, it eventually becomes unnecessary to include high-ionization stages. As we discard them, starting from the highest ones, we can lower the floor temperature and not face the floating-point-errors we would otherwise get in the evaluation of exponentials. In practice, we use a floor temperature of 2000–4000 K during the plateau phase, lowered to 1000-2000 K during the nebular phase. A lower floor temperature, or none at all, would be more suitable. Indeed, our tests suggest that this is in part the reason for the overestimated flux in the UV and *UB* bands.

The spatial grid used for the radiative-transfer solution is set to have (approximately) a constant increment in optical-depth (computed using the Rosseland-mean opacity), with typically five points per optical-depth decade, and a maximum of 100 points. This is much less than the original 750–900 data points of the hydrodynamical-input grid. However, our grid is much finer for the regions where radiation decouples from matter, the transition from Eddington factors of 1/3 to 1 occurs over a few tens of points, while in the hydro input this transition takes place over merely a few points. Furthermore, as the ejecta recombine, our grid adjusts to track the recombination fronts (across which the optical depth varies steeply with radius). In SNe II, three main fronts form, associated with the recombination to He II, He I and H I. However, these fronts never steepen as fiercely as in our simulations of SN1987A (Dessart & Hillier 2010) or as in steady-state SNe II-P simulations (e.g. Dessart et al. 2008). Convergence is not inhibited by this feature and is indeed quite steady in the simulations we describe here.

For the treatment of radioactive decay, we assume only one decay chain corresponding to ^{56}Ni $\rightarrow$ ^{56}Co $\rightarrow$ ^{56}Fe. In a forthcoming paper, we will present a Monte Carlo code that solves for the transport of γ-ray photons from the site of emission out through the ejecta and potentially towards escape. We find that in SNe II, the deep-seated location of nucleosynthesized ^{56}Ni and the large overlying mass prevent the escape of γ-ray photons up to $\gtrsim$500 d. Non-local energy deposition starts, however, to operate at a few hundred days. As the ejecta become thin to optical photons near the end of the photospheric phase, high-energy (i.e. non-thermal) electrons, Compton-scattered by γ-rays, will affect the excitation and ionization level of the gas.

A proper and accurate treatment of radioactive decay requires first the determination of the energy deposition versus depth (Ambwani & Sutherland 1988; Swartz, Sutherland & Harkness 1995), and second the heating/excitation/ionization effects of the high-energy electrons produced (Axelrod 1980; Lucy 1991; Swartz 1991; Kozma & Fransson 1992; Swartz et al. 1993; Kozma & Fransson 1998a,b). Although aware of these important issues, we assume in this first study of SNe II-P that all decay energy is deposited locally as heat. We anticipate this will overestimate the SN visual brightness at nebular times, and underestimate the excitation/ionization level of the gas. In our simulations, this neglect seems to affect primarily hydrogen, causing Balmer lines and the associated continuum to vanish abruptly beyond $\sim$130 d after explosion, contrary to observations (see Section 7).

3 MODEL ATOMS, ATOMIC DATA AND DEPARTURES FROM LTE

The model atoms used in our simulations are similar to those adopted in Dessart & Hillier (2010). The choice is a compromise between physical accuracy, completeness and computational burden. Our simulations require about 6 GB of RAM and one time-step takes about 2–3 d on a single CPU. In CMFGEN, we can in principle treat all species up to $Z = 28$ (Nickel), as well as Barium ($Z = 56$). However, to limit the computational burden, our early CMFGEN simulations based on models s15e12/s25e12 neglected some species and/or ions. In Table 3, we document these details, including for each ion species the number of super and full levels, the number of transitions and the uppermost level included.[1] To capture the higher level of detail of the ejecta composition for model s15e12iso and compute more accurate spectra for comparison with observations, we additionally include in our treatment Ne II, Al II, Al III, Ar III, Sc I, Sc II, Sc III, Cr II, Cr III, Fe I, Ni II, Ni III, Ni IV, Ba I and Ba II (these additional ions appear with a superscript *a*). As we discuss below, our simulations based on s15e12iso show the importance of treating Na I, Sc II, Cr II and Fe I, as well as considering the corresponding elemental abundance stratification with depth.

The model atoms described in Table 3 are used to start the time sequences. As time proceeds, the ejecta recombine and cool so that the highest ionization species can progressively be discarded. During the nebular phase, our model atom typically contains species that are at most three-times ionized. Concomitantly, the low density and weaker radiation field at late times favour the appearance of forbidden lines (associated with Ca II and O I in particular). We therefore adapt the super-level assignment to capture this change in conditions as ions get less and less excited. In practice, past 100–200 d, we typically split the lower 10 super levels for all species (splitting the lower 20 super levels does not alter the results visibly and supports this choice). The set of atomic processes, most of the atomic data and their use have been summarized in Dessart & Hillier (2010) and discussed in more detail in Hillier & Miller (1998); they are thus not repeated here. For Ba II, not included in earlier models, we used the atomic data discussed by Mazzali, Lucy & Butler (1992) (kindly supplied by K. Butler), while for Sc II and Sc III we used oscillator strengths from Kurucz (2009)[2] and crude approximations for the photoionization cross-sections. Energy levels, when available, were taken from NIST.[3]

3.1 Departure coefficients

In Fig. 3, we show the departure coefficients as a function of the Rosseland-mean optical depth ($\tau_{\rm Rosseland}$) for H I, O I and Fe II at two different epochs. These departure coefficients are defined as the ratio of the non-LTE population to the LTE population, where the LTE population has been computed using the electron temperature, and the actual values of the ion and electron densities. As expected, LTE is recovered at large optical depth ($\tau_{\rm Rosseland} > 10$). Below $\tau_{\rm Rosseland} = 10$, significant departures from LTE begin to occur, and these are well developed around the photospheric layers. At small optical depths, the departure from LTE can be orders of magnitude.

[1] Level designations are generally according to the National Institute of Standards and Technology (NIST), except we use 'z' to refer to states where several high 'l' states have been merged (say $l = 4$ to $n - 1$), and 'w' states refer to a level where all 'l' states for a given multiplicity have been merged.
[2] Data are available online at http://kurucz.harvard.edu
[3] Data are available online at http://physics.nist.gov/asd3

© 2010 The Authors, MNRAS **410,** 1739–1760
Monthly Notices of the Royal Astronomical Society © 2010 RAS

Downloaded from https://academic.oup.com/mnras/article/410/3/1739/962985 by CNRS - ISTO user on 30 November 2021

Table 3. Summary of the complete model atom used in our radiative-transfer calculations for model s15e12iso (our simulations for models s15e12 and s25e12 were done without the species identified with superscript *a*). The source of the atomic data sets is given in Dessart & Hillier (2010). N_f refers to the number of full levels, N_s to the number of super levels and N_{trans} to the corresponding number of bound–bound transitions. The last column refers to the upper level for each ion treated. The total number of full levels treated is 8273, which corresponds to 173 965 bound–bound transitions.

Species	N_f	N_s	N_{trans}	Upper level
H I	30	20	435	$n \leq 30$
He I	51	40	374	$n \leq 11$
He II	30	13	435	$n \leq 30$
C I	26	14	120	$n \leq 2s2p^3\ ^3P^o_0$
C II	26	14	87	$n \leq 2s^24d\ ^2D_{5/2}$
C III	112	62	891	$n \leq 2s8f\ ^1F^o$
C IV	64	59	1446	$n \leq 30$
N I	104	44	855	$n \leq 5f\ ^2F^o$
N II	41	23	144	$n \leq 2p^3d\ ^1P_1$
O I	51	19	214	$n \leq 2s^22p^3(^4S)4f\ ^3F_3$
O II	111	30	1157	$n \leq 2s^22p^2(^3P)4d\ ^2D_{5/2}$
O III	86	50	646	$n \leq 2p4f\ ^1D$
O IV	72	53	835	$n \leq 2p^2(^3P)3p\ ^2P$
O V	78	41	523	$n \leq 2s5f\ ^1F^o_3$
Ne II[a]	242	42	5794	$n \leq 2s^22p^4\ ^1D\ 4d\ ^2S$
Na I	71	22	1614	$n \leq 30w\ ^2W$
Mg II	65	22	1452	$n \leq 30w\ ^2W$
Al II[a]	44	26	171	$n \leq 3s5d\ ^1D_2$
Al III[a]	45	17	362	$n \leq 10z\ ^2Z$
Si II	59	31	354	$n \leq 3s^2(^1S)7g\ ^2G_{7/2}$
Si III	61	33	310	$n \leq 3s5g\ ^1G_4$
Si IV	48	37	405	$n \leq 10f\ ^2F^o$
S II	324	56	8208	$n \leq 3s3p^3(^5S^o)4p\ ^6P$
S III	98	48	837	$n \leq 3s3p^2(^2D)3d\ ^3P$
S IV	67	27	396	$n \leq 3s3p(^3P^o)4p\ ^2D_{5/2}$
Ar III[a]	346	32	6898	$n \leq 3s^23p^3(^2D^o)8s\ ^1D^o$
Ca II	77	21	1736	$n \leq 3p^630w\ ^2W$
Sc I[a]	72	26	734	$n \leq 3d4s(^3D)5s\ ^2D_{5/2}$
Sc II[a]	85	38	979	$n \leq 3p^63d4f\ ^1P_1$
Sc III[a]	45	33	235	$n \leq 7h\ ^2H_{11/2}$
Ti II	152	37	3134	$n \leq 3d^2(^3F)5p\ ^4D_{7/2}$
Ti III	206	33	4735	$n \leq 3d6f\ ^3H^o_6$
Cr II[a]	196	28	3629	$n \leq 3d^4(^3G)4p\ x^4G_{11/2}$
Cr III[a]	145	30	2359	$n \leq 3d^3(^2D2)4p\ ^3D^o_3$
Fe I[a]	136	44	1900	$n \leq 3d^6(^5D)4s4p\ x^5F^o_3$
Fe II	115	50	1437	$n \leq 3d^6(^1G1)4s\ d^2G_{7/2}$
Fe III	477	61	6496	$n \leq 3d^5(^4F)5s\ ^5F_1$
Fe IV	294	51	8068	$n \leq 3d^4(^5D)4d\ ^4G_{5/2}$
Fe V	191	47	3977	$n \leq 3d^3(^4F)4d\ ^5F_3$
Fe VI	433	44	14103	$n \leq 3p5(^2P^o)3d^4(^1S)\ ^2P_{3/2}$
Fe VII	153	29	1753	$n \leq 3p5(^2P^o)3d^3(^2D1)\ ^1P_1$
Co II	144	34	2088	$n \leq 3d^6(^5D)4s4p\ ^7D^o_1$
Co III	361	37	10937	$n \leq 3d^6(^5D)5p\ ^4P_{3/2}$
Co IV	314	37	8684	$n \leq 3d^5(^2P)4p\ ^3P_1$
Co V	387	32	13605	$n \leq 3d^4(^3F)4d\ ^2H_{9/2}$
Co VI	323	23	9608	$n \leq 3d^3(^2D)4d\ ^1S_0$
Co VII	319	31	9096	$n \leq 3p5(^2P^o)3d^4(^3F)\ ^2D_{3/2}$
Ni II[a]	93	19	842	$n \leq 3d^7(^4F)4s4p\ ^6D^o_{1/2}$
Ni III[a]	67	15	379	$n \leq 3d^7(^4F)4p\ ^3D^o_1$
Ni IV[a]	200	36	4085	$n \leq 3d^6(^3D)4p\ ^2D_{5/2}$
Ni V	183	46	3065	$n \leq 3d^5(^2D3)4p\ ^3F^o_3$
Ni VI	314	37	9569	$n \leq 3d^4(^5D)4d\ ^4F_{9/2}$
Ni VII	308	37	9225	$n \leq 3d^3(^2D)4d\ ^3P_2$
Ba I[a]	31	17	30	$n \leq 5d6p\ ^1P_1$
Ba II[a]	100	38	2514	$n \leq 3s30w\ ^2W$

In general, the behaviour of the departure coefficients is complex, and highly dependent on the level under consideration.

The very significant departures of the populations from their LTE values is not surprising. In general electron scattering and line scattering dominate the opacity, and these do not strongly couple the radiation field with the electron temperature. Further, the electron density is low at the photosphere ($\sim 10^{10}$ cm^{-3}), and hence collisions are generally ineffective at causing a significant coupling of the majority of the level populations and ionization state of the gas, and cannot overcome their stronger coupling with the radiation field.

Above the photosphere the electron temperature is strongly decoupled from the radiation field temperature, and is instead determined by an equilibrium between many different processes, including adiabatic cooling, collisional cooling and heating, and heating by photoionization. Indeed, at the outer boundary of s15e12iso at, e.g. $\sim$50 d, the temperature has reached the floor value of 3000 K, while the photospheric temperature is somewhat lower than 6000 K. If we assume that the ground-state population is determined by the radiation temperature, we would expect a departure coefficient of order $\exp(157,850/T_{rad} - 157,850/T_e)$ or $\sim 3.0 \times 10^{-12}$ assuming $T_e = 3000$ K, $T_{rad} = 6000$ K and a fixed electron density; hence very small departure coefficient for the lower levels are to be expected. Of course, the situation is more complex than assumed above – the radiation field is a diluted blackbody, and in the outer regions the H ionization is not in equilibrium because the recombination time-scale is longer than the expansion time-scale.

For H I, the departure coefficients are close to unity for high principal quantum number, as expected. For Fe II, all the levels shown have very small departure coefficients at low $\tau_{Rosseland}$. This is not surprising – although we have shown 115 levels (with a smaller number of super levels), the principal quantum number of the valence electron for levels illustrated is less than 5. For Fe II the lower metastable levels are coupled by collisions with the ground state, and hence tend to be in LTE with respect to the ground state (i.e. they have the same departure coefficient as the ground state). This can be seen in Fig. 3 – many levels have similar departure coefficients around $\tau_{Rosseland} = 1$. A similar statement applies to metastable levels of other elements.

In Monte Carlo simulations of SN spectra it is common practice to use approximate formula to determine the ionization structure, and to use an LTE assumption to determine populations (e.g. Kasen, Thomas & Nugent 2006; Kasen & Woosley 2009). As the photon scattering is treated explicitly, the calculations are neither LTE nor rigorously non-LTE. As apparent from the above, and indeed from our need to explicitly allow for the time-dependence when solving for the hydrogen ionization structure, non-LTE populations need to be allowed for when modelling Type II SN. Experience indicates that as we include more processes, more lines and more levels, the departures from LTE will probably become smaller, but the departures will still be highly significant.

4 EJECTA EVOLUTION

Over the 10–1000 d covered by each simulation, the ejectum expands by two orders of magnitude and changes from being rather dense and optically thick to being very tenuous and optically thin. Over the same time period, the ejectum cools from a few 10^5 K at depth, to temperatures everywhere less than 3000 K. These dramatic changes cause an equivalently dramatic change in the radiated light, which we describe in Sections 5 and 6.

Downloaded from https://academic.oup.com/mnras/article/410/3/1739/962985 by CNRS - ISTO user on 30 November 2021

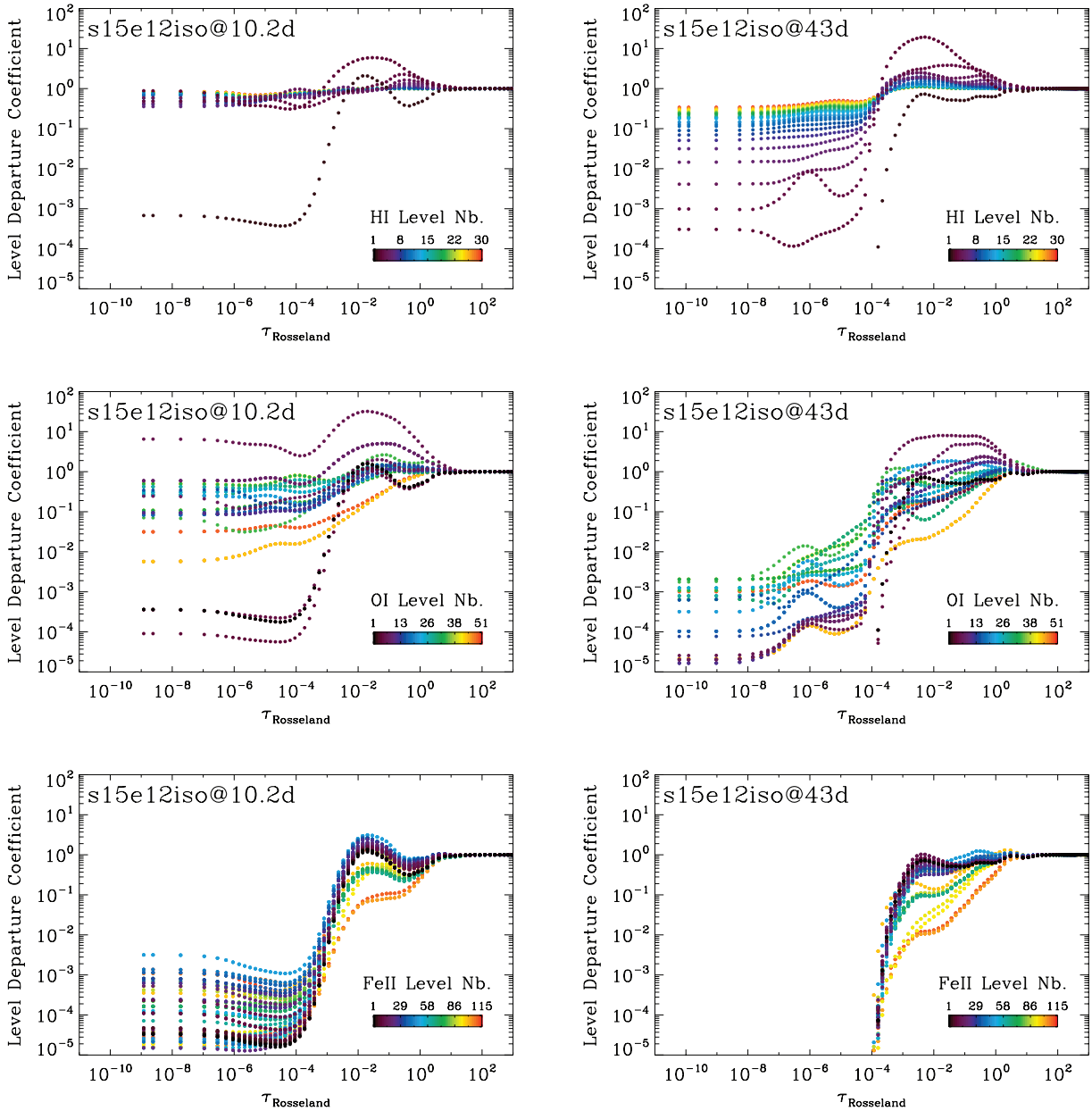

Figure 3. Left column: variation of the departure coefficients of H I (top), O I (middle) and Fe II levels versus Rosseland optical depth for models s15e12iso at 10.2 d after shock breakout. Right column: same as left, but for the model s15e12iso at 43 d after shock breakout. Non-LTE level populations computed in our simulations match closely their LTE counterpart only in regions where the Rosseland mean optical depth is greater than a few. Non-LTE prevails everywhere else.

During the photospheric phase, the electron-scattering radial optical depth is, by definition, greater than a few. Thus, during this phase there always exists a 'photosphere', which we formally define as the location where that optical depth is 2/3. The behaviour of the photosphere determines to a large extent the SN light curve, and we illustrate the evolution of its properties in Fig. 4. Starting $\gtrsim$10 d past explosion, our simulations miss the phase of rapid evolution of photospheric properties which immediately follows shock breakout (Dessart et al. 2008; Gezari et al. 2008; Tominaga et al. 2009; Rabinak & Waxman 2010). Indeed, at the start of our simulations, the photosphere has already expanded by about a factor of 10, its temperature dropped to $\lesssim$10 000 K and its velocity has been reduced to $\lesssim$8500 km s^{-1}. Subsequently, for each simulation, and over the first ~80 d, we find a slow decrease of the photospheric temperature and velocity, but a systematic increase in radius.

Importantly, the photosphere resides within the outer 0.5 M$_\odot$ of the ejecta for about ~50 d after the explosion (Fig. 5). Over that initial expansion, the ejecta has sufficient thermal energy to remain ionized while expanding, so that the photosphere remains close to the progenitor surface layers. As recombination sets in during the plateau phase, the photosphere eventually recedes in mass, but this recession is initially compensated by expansion so that the change in photospheric radius is small – in the present models the photospheric radius only begins to shrink after ~80 d.

The photospheric composition does not change for the first ~70 d in these two SNe II-P models and is identical to that of the progenitor

Downloaded from https://academic.oup.com/mnras/article/410/3/1739/962985 by CNRS - ISTO user on 30 November 2021

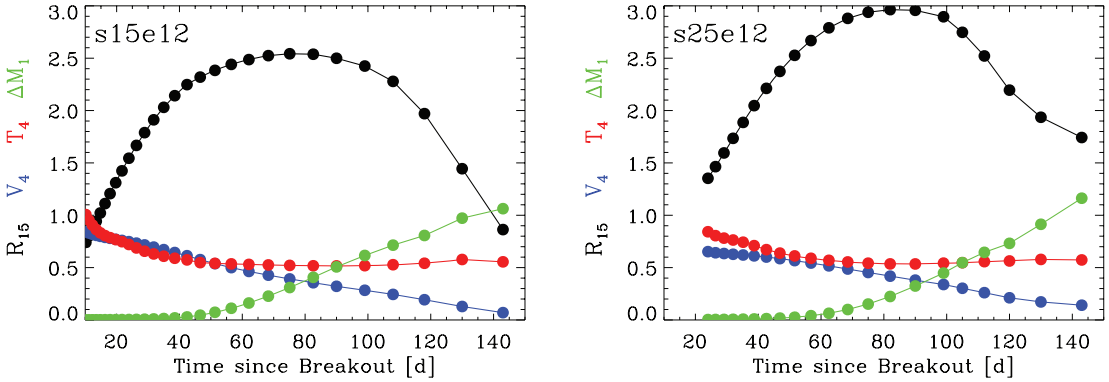

Figure 4. Evolution of the photospheric radius R_{15} (black; $R_{15} = R_{\rm phot}/10^{15}$ cm), photospheric velocity V_4 (blue; $V_4 = V_{\rm phot}/10^4\,{\rm km\,s^{-1}}$), photospheric temperature T_4 (red; $T_4 = T_{\rm phot}/10^4$ K) and the mass above the photosphere ΔM_1 (green; $\Delta M_1 = \Delta M_{\rm phot}/10\,{\rm M_\odot}$) until 150 d after explosion, and shown for simulations based on model s15e12 (left) and s25e12 (right). The dots correspond to the actual times at which the radiation-transfer simulations were performed. The evolution at nebular times is excluded since no photosphere exists at such epochs.

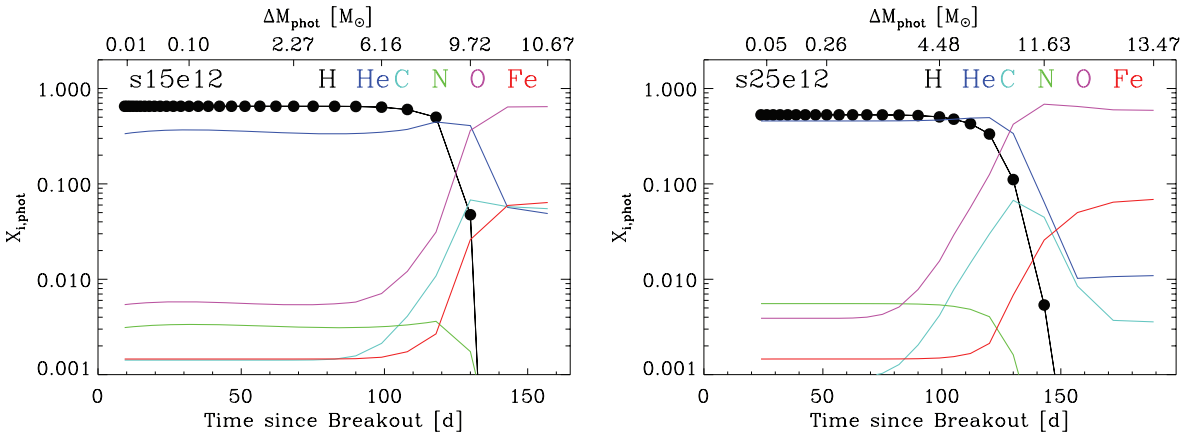

Figure 5. Evolution of the composition at the photosphere for a few important species in our simulations based on models s15e12 (left) and s25e12 (right). The dots give the epoch for each simulation in the time sequence, and $\Delta M_{\rm phot}$ in Fig. 5 is the mass contained between the photosphere and the outer-model boundary. Notice the coincidence of the end of the plateau phase (shown further below in Fig. 9) with the recession of the photosphere into the helium-rich (hydrogen-poor) layers of the ejecta.

surface. The same finding by Eastman et al. (1994) suggests that this is a generic property of SNe II-P. It implies that the spectral evolution of SNe II-P during the first half of the plateau phase does not stem from composition changes, but instead from changes in ionization. The same applies to the early evolution of SN1987A (Dessart & Hillier 2010).

The near uniform photospheric composition with time during the photospheric phase, as well as the modest composition contrast between the hydrogen envelopes of RSG models (see e.g. Woosley et al. 2002 or Woosley & Heger 2007), highlights the difficulty of constraining the progenitor identity with photospheric-phase spectra. It also partially explains the uniformity of SNe II-P spectra, which tend to show lines from the same ions, with the same strength and shapes, and generally only differing in width (Dessart & Hillier 2006; Dessart et al. 2008). This suggests that differences between SNe II-P are difficult to extract after the onset of recombination in the photospheric phase. They may instead be constrained from early time observations, when the photospheric regions are partially ionized (Dessart & Hillier 2006; Baron et al. 2007), or from nebular-phase observations during which the progenitor core, whose properties differ greatly with progenitor main-sequence mass, is revealed (Woosley et al. 2002; Dessart et al. 2010a).

The location of the SN II-P photosphere in the outer $\lesssim 1\,{\rm M_\odot}$ of the ejecta suggests that a mass buffer of $\sim 10\,{\rm M_\odot}$ of material separates the radiating layer from the birth place of the explosion. As long as the photosphere remains in those outer ejecta shells, which seems to be during the first half of the plateau phase, radioactive decay cannot influence the emergent radiation of SNe II-P. Altogether, these properties give support to the notion that distance determinations to SNe II-P using spectroscopy are best determined from early- rather than late-time observations (Baron et al. 2007; Dessart et al. 2008; Dessart & Hillier 2009).

A comparison with simulations of SN1987A (Dessart & Hillier 2010) illustrates further the ingredients controlling the behaviour of the photosphere. At early post-breakout times, the rapid recombination of the highly ionized fast-expanding outer ejecta leads to a steep decrease of the photospheric velocity (Fig. 6). In SNe II-pec, this fast decrease is caused in part by the relatively small progenitor-star radius, and it slows down only when the photosphere reaches the inner ejecta heated by decay energy (at $\sim$30 d in SN1987A). In SNe II-P, a similar, albeit more modest, decrease in photospheric velocity is seen at early times (Gezari et al. 2008), but it slows down as recombination sets in. A rapid decrease kicks in again when the photosphere reaches the base of the hydrogen envelope (at $\gtrsim$100 d in the two present simulations).

Downloaded from https://academic.oup.com/mnras/article/410/3/1739/962985 by CNRS - ISTO user on 30 November 2021

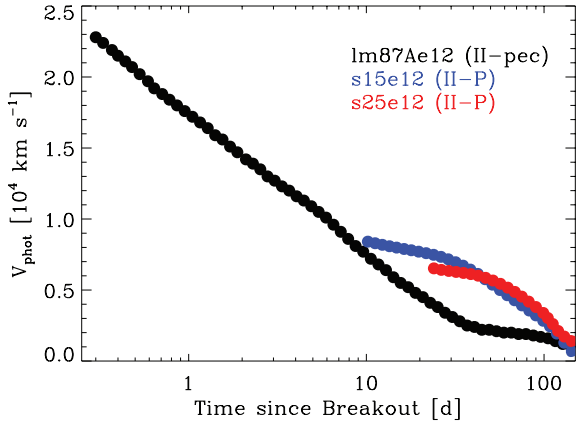

Figure 6. Evolution of the photospheric velocity obtained with our simulations based on SNe II-P models s15e12 and s25e12 (blue and red lines; this work) and the SN II-pec model lm87Ae12 of SN1987A (black line; Dessart & Hillier 2010).

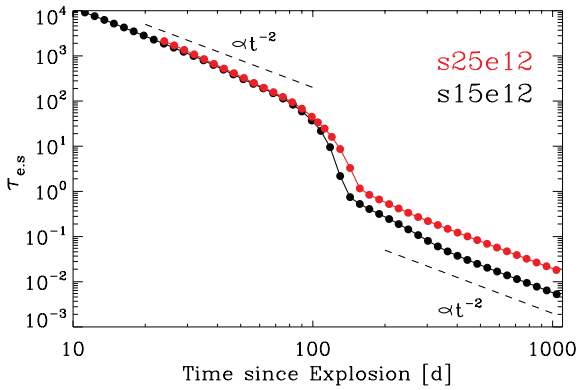

Figure 7. Evolution of the electron-scattering optical depth at the base of the ejecta for the simulations based on models s15e12 (black) and s25e12 (red). Dots represent the epochs at which our computations are carried out. We draw a line of $1/t^2$ slope, which gives the rate of change of the optical depth for a homologously expanding gas of non-changing ionization. The faster decline that we obtain in both simulations is caused by ionization changes (i.e. recombination, and primarily of hydrogen), while the step at ∼100 d is caused by a composition change as the photosphere enters the hydrogen-deficient helium-rich core.

Compared to our analyses of SNe II-P 1999em and 2006bp (Dessart & Hillier 2006; Dessart et al. 2008), characterized by explosion energies close to but likely larger than the 1.2 B value of our models (Utrobin 2007; Dessart et al. 2010a), the photospheric quantities we obtain with these two sets of simulations are in good agreement with the temperature and the velocity. However, our models reach larger maximum radii of 2.5–3 × 10^{15} cm, compared to ∼1.6 × 10^{15} cm (Dessart et al. 2008). We speculate on the origin of this discrepancy in Section 7.

As the homologously expanding SN evolves through the plateau phase, the ejecta electron-scattering optical depth decreases (Fig. 7). It does so initially at constant ionization, so its rate of decline follows a $1/t^2$ slope, but as recombination sets in after a few weeks, this rate becomes steeper. At about 100 d after explosion, the optical depth suddenly declines much faster in both simulations, as the photosphere enters the hydrogen-deficient helium-rich regions of the ejecta, which possess a higher mean-atomic weight and hence a smaller mass-absorption coefficient.

Table 4. Summary of photospheric-phase properties for the non-LTE time-dependent simulations based on model s15e12. For each epoch, we give the total ejecta electron-scattering optical depth, the photospheric radius (in 10^{15} cm), the photospheric velocity (in km s^{-1}), the photospheric temperature (in K), the amount of mass above the photosphere (ΔM_{phot}, given in M$_\odot$), as well as the emergent bolometric luminosity (in 10^8 L$_\odot$). Results for the time-sequence based on s15e12iso are the same as for those based on s15e12, and hence are not shown here.

			s15e12			
Age (d)	$\tau_{base,es}$	R_{phot} (10^{15} cm)	V_{phot} (km s^{-1})	T_{phot} (K)	ΔM_{phot} (M$_\odot$)	L_{bol} (10^8 L$_\odot$)
9.30	14034.20	0.69	8545	10661	0.008	7.94
10.20	11053.89	0.74	8406	10063	0.010	7.64
11.20	9134.01	0.80	8294	9527	0.011	7.54
12.30	7567.96	0.87	8183	9057	0.014	7.50
13.50	6259.40	0.94	8083	8642	0.016	7.44
14.80	5192.15	1.02	7988	8317	0.019	7.37
16.30	4252.72	1.11	7890	8054	0.023	7.24
17.90	3490.37	1.21	7800	7859	0.027	7.11
19.70	2823.76	1.31	7701	7678	0.032	6.96
21.70	2287.51	1.42	7595	7477	0.038	6.78
23.90	1863.47	1.54	7480	7208	0.046	6.65
26.30	1519.30	1.67	7337	6878	0.057	6.56
28.90	1233.58	1.79	7164	6564	0.075	6.49
31.80	993.68	1.91	6957	6305	0.101	6.42
35.00	796.48	2.03	6715	6087	0.141	6.35
38.50	630.28	2.14	6438	5893	0.200	6.30
42.40	495.07	2.25	6135	5735	0.290	6.29
46.60	388.62	2.32	5760	5478	0.455	6.19
51.30	304.74	2.38	5378	5403	0.733	6.19
56.50	240.12	2.44	4999	5355	1.118	6.15
62.10	190.81	2.49	4634	5306	1.619	6.03
68.30	149.01	2.52	4277	5255	2.274	5.85
75.10	113.56	2.54	3918	5211	3.097	5.61
82.60	83.02	2.54	3556	5174	4.071	5.32
90.00	58.83	2.50	3214	5162	5.069	5.02
99.00	37.12	2.43	2835	5185	6.159	4.52
108.00	21.80	2.28	2441	5276	7.144	3.98
118.00	9.53	1.97	1932	5415	8.069	3.31
130.00	2.19	1.44	1286	5775	9.723	2.18
143.00	0.75	0.86	698	5550	10.628	1.11

The photosphere vanishes when the total ejecta electron-scattering optical depth drops below 2/3 (last entry in Tables 4 and 5) and the SN enters the nebular phase. The ejecta are optically thin initially in the optical continuum, although not yet in the lines. All ejecta mass shells are visible, with emission biased towards the denser/hotter inner layers. During the nebular phase, the maximum electron density decreases to values on the order of 10^5–10^6 cm^{-3}, and forbidden lines such as [O I] 6303–6363 Å and [Ca II] 7291–7323 Å become strong. The nebular ejecta does not change its ionization much with time, and the rate of change of the now very low electron-scattering optical depth follows approximately a $1/t^2$ slope. For completeness, we show the full evolution of the ejecta temperature and electron density over the whole time sequence for the simulation based on model s15e12 in Fig. 8.

5 SYNTHETIC BOLOMETRIC LUMINOSITY AND LIGHT CURVES

In Fig. 9, we show the bolometric luminosity for each time sequence from 10 to 20 d until about 1000 d after the explosion. As

© 2010 The Authors, MNRAS **410,** 1739–1760
Monthly Notices of the Royal Astronomical Society © 2010 RAS

Downloaded from https://academic.oup.com/mnras/article/410/3/1739/962985 by CNRS - ISTO user on 30 November 2021

Table 5. Same as Table 4, but now for the time sequence based on model s25e12.

			s25e12			
Age (d)	$\tau_{\rm base,es}$	$R_{\rm phot}$ (10^{15} cm)	$V_{\rm phot}$ (km s^{-1})	$T_{\rm phot}$ (K)	$\Delta M_{\rm phot}$ (M$_\odot$)	$L_{\rm bol}$ (10^8 L$_\odot$)
24.0	2124.66	1.35	6524	8423	0.040	12.64
26.4	1709.78	1.46	6419	8050	0.048	11.87
29.1	1356.11	1.60	6344	7815	0.057	11.50
32.0	1080.90	1.73	6274	7635	0.067	11.21
35.2	849.14	1.89	6203	7426	0.080	10.91
38.7	665.03	2.05	6121	7097	0.098	10.55
42.6	523.98	2.21	6009	6714	0.128	10.19
46.9	414.59	2.37	5858	6385	0.179	9.81
51.6	324.49	2.53	5668	6116	0.263	9.42
56.8	251.96	2.67	5437	5889	0.405	9.05
62.5	197.03	2.79	5166	5696	0.639	8.69
68.5	157.38	2.88	4866	5540	0.997	8.33
75.0	123.25	2.94	4535	5422	1.518	7.98
82.0	94.47	2.96	4183	5354	2.243	7.64
90.0	67.84	2.96	3803	5349	3.244	7.28
99.0	45.06	2.90	3385	5427	4.480	6.86
105.0	33.80	2.75	3028	5467	5.473	6.55
112.0	24.62	2.52	2605	5571	6.457	5.98
120.0	16.11	2.19	2117	5633	7.317	5.43
130.0	8.67	1.94	1723	5781	9.138	4.81
143.0	3.30	1.74	1410	5732	11.628	3.22
157.0	1.16	1.57	1154	5434	12.923	1.91
172.0	0.84	1.03	693	5270	13.365	1.51
189.0	0.66	0.39	238	5181	13.473	1.30

expected for the explosion of RSG progenitors, the initial photospheric phase is characterized by a quasi-plateau luminosity, with a length on the order of 100–150 d. The longer plateau duration in the simulation based on model s25e12 is caused in part by the larger production of ^{56}Ni during the explosion (i.e. 0.163 M$_\odot$) compared to that in model s15e12 (0.0866 M$_\odot$). The bolometric luminosity decreases at the end of the plateau phase and meets the (dashed) curve representing the energy-production rate through radioactive decay at ∼140 d (160 d) for the simulation based on model s15e12 (s25e12).[4]

In our models the fading from the plateau is not abrupt, but instead takes about a month, and corresponds to a luminosity decrease by a factor of a few. We find that this prolonged fall-off is in part an artefact of the large time-step of ∼12 d (i.e. 10 per cent of 120 d) in our simulations at such times. Recomputing this phase with CMFGEN using a finer and constant time increment of 2 d yields a faster fading of ∼10 d but still gives the same fading magnitude (Fig. 10). Our neglect of light-travel-time effects is secondary here, since it would only produce a smearing of the bolometric luminosity over a time-scale of $\lesssim$1 d. Comparison between the evolution of the bolometric luminosity and the composition at the photosphere (Figs 5 and 9) indicates that the plateau or high-brightness phase of the SN corresponds to the epoch during which the photosphere resides within the hydrogen-rich region of the SN ejecta. As soon as the photosphere reaches the outer edge of the helium core, the plateau brightness ebbs. The subsequent light-curve evolution is qualitatively similar in both models, suggesting little sensitivity to

[4] The decay-energy production rate shown in Fig. 9 corresponds to the average energy produced per time interval, and thus differs from the instantaneous value at a given post-explosion time.

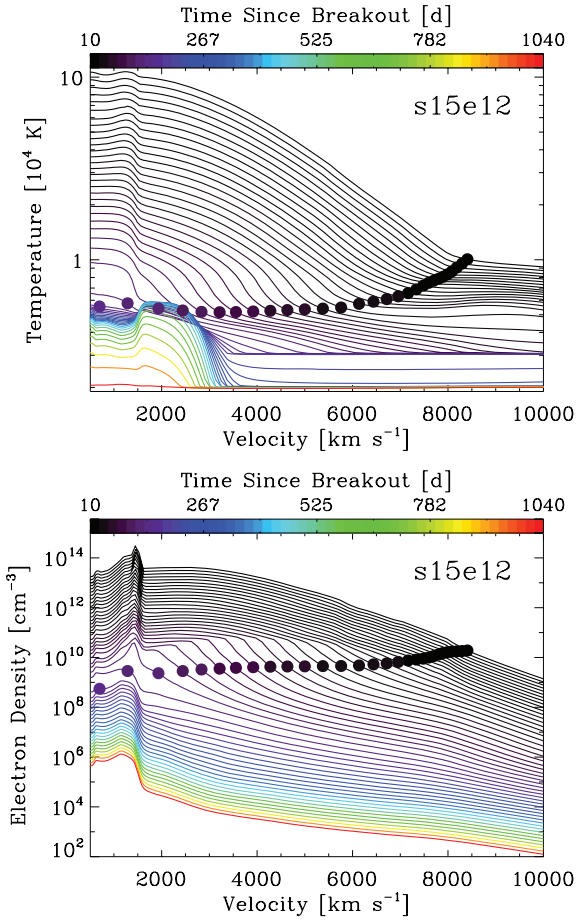

Figure 8. Top: evolution of the ejecta gas temperature from 10 to 1040 d after explosion in the simulations based on model s15e12. Dots give the position of the photosphere, which by definition exists as long as the base electron-scattering optical depth is greater than 2/3. A colour coding is used to differentiate the epochs. Bottom: same as top, but now showing the electron density.

the differing helium-core masses (4.27 M$_\odot$ in model s15e12 and 8.19 M$_\odot$ in model s25e12).

Bolometric light curves for four SN II-P (SN1999em, SN2003gd, SN2004et, SN2005cs) are presented by Smartt (2009). All four show a drop of around 1 mag close to 120 d from maximum, and for one of them (SN 2005cs) the bolometric luminosity changes by almost a factor of 2 on a time-scale of ∼10 d, while for SN1999em the change is more gradual. As the end of the plateau phase is determined by the transition of the photosphere from the hydrogen-rich envelope to the helium core, the steepness of the change will depend on any mixing that has occurred between these layers, as well any departure from spherical symmetry.

The bolometric luminosity for the simulation based on model s25e12 is greater at all times than for the simulation based on model s15e12. The larger plateau brightness stems from the larger progenitor radius in model s25e12, while the larger nebular flux is caused by the larger amount of ^{56}Ni produced by the explosion in model s25e12. The magnitude of the fading at the end of the plateau is thus a function of both the progenitor size and the amount of ^{56}Ni produced. As the progenitor radius and mass of nucleosynthesized ^{56}Ni are unlikely to be fundamentally related (because of the influence of abundance variations, rotation, binary evolution and the complexities of the explosion mechanism), there should be no clear

Downloaded from https://academic.oup.com/mnras/article/410/3/1739/962985 by CNRS - ISTO user on 30 November 2021

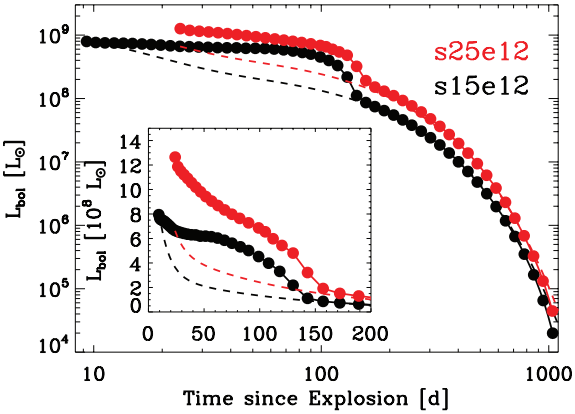

Figure 9. Main panel: log–log plot of the evolution of the bolometric luminosity for our simulations based on models s15e12 (black; model contains 0.0866 $M_\odot$ of ^{56}Ni initially) and s25e12 (red; model contains 0.163 $M_\odot$ of ^{56}Ni initially). Dots indicate the time of each computation. We also overplot as a dashed line the mean γ-ray energy released per time interval, computed independently for each model using our Monte Carlo code (see Hillier & Dessart in prep.), and assumed in this set of calculations to be deposited locally as a heat source (we do not treat non-thermal ionization/excitation). Note that due to computation over different time intervals, the solid/dashed curves diverge somewhat at very late times, when time increments are large and of the order of 100 d. Inset: same as main panel, but now zooming-in on the plateau phase and the onset of the nebular phase. We now use a linear scale for both axes.

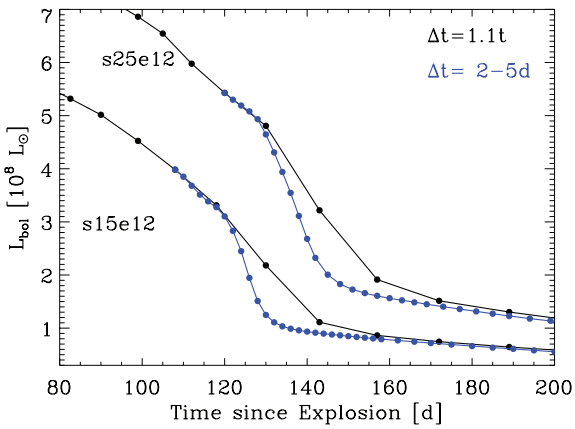

Figure 10. Same as Fig. 9 for models s15e12 and s25e12, but now comparing results from CMFGEN when we adopt a time increment of 10 per cent of the current time (black; this is our standard choice already shown in Fig. 9, which yields large time-steps at late times), or a constant time increment of 2 to 5 d (blue curves). For each curve, the dots give the times at which the CMFGEN calculations were carried out. Using a fixed and finer time increment yields a different result at the end of the plateau phase, which is better resolved and found to last about 10 d in both models.

correlation between plateau and nebular brightness, and thus the observed post-plateau fading should show a large scatter. The approximate treatment of radioactive decay in this study cannot alter this result since no γ-rays are predicted to escape up to $\gtrsim$500 d. At later times, our neglect of γ-ray photon escape will lead to an overestimate of the bolometric luminosity shown here, by up to a factor of 2 at 1000 d.

The bolometric luminosity is not directly observable because not all spectral bands are accessible. Moreover, filter bandpasses are separated by gaps, sometimes sizeable, that miss regions of

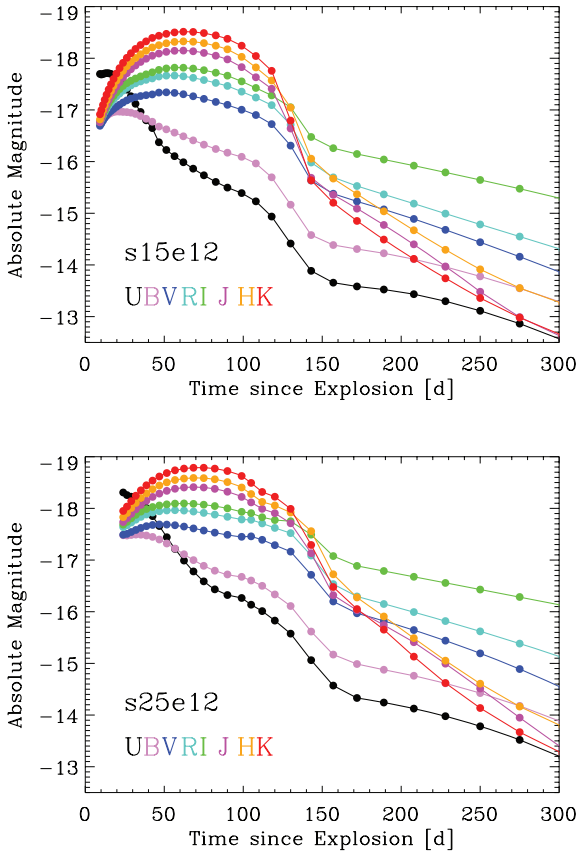

Figure 11. Top: synthetic optical and near-IR light curves for the simulation based on model s15e12 and obtained by integrating our non-LTE time-dependent spectra at each epoch over the filter-transmission functions of Landolt (1992) and Cohen, Wheaton & Megeath (2003). Bottom: same as top, but now for the simulation based on model s25e12. Dots indicate the time of each computation.

non-zero flux (and potentially strong lines). Regions of intense atmospheric absorption prevent the observation of certain spectral regions altogether, as in some parts of the near-infrared (near-IR). Hence, in Fig. 11, we show multi-band synthetic photometry for our two simulations based on models s15e12 and s25e12. These are obtained by integrating our non-LTE time-dependent synthetic spectra at each epoch with the filter transmission functions of Landolt (1992) for the optical bands, and with those of Cohen et al. (2003) for the near-IR bands.

While the bolometric luminosity shows a steady and slow decline at most epochs, the multi-band light curves show a contrasting behaviour affected by ejecta cooling. In particular, the photospheric cooling after shock breakout leads to a continuous decrease of the flux at short wavelengths, as the peak of the distribution sweeps through the far-UV, to the UV, and approaches the optical bands (Gezari et al. 2008). This translates here into a 'bell' shape for the *B*-band light curve, but a plateau followed by a steady fading in the *U* band. In contrast, the *VRIJHK* magnitudes all rise at all times prior to about 50 d after explosion, before turning over and declining. Both simulations based on models s15e12 and s25e12 show a similar behaviour, the latter being visually brighter at all photospheric and nebular epochs. As discussed previously, this contrast stems from the larger progenitor radius, and the larger amount of ^{56}Ni produced in model s25e12.

© 2010 The Authors, MNRAS **410,** 1739–1760
Monthly Notices of the Royal Astronomical Society © 2010 RAS

Downloaded from https://academic.oup.com/mnras/article/410/3/1739/962985 by CNRS - ISTO user on 30 November 2021

Besides differences in progenitor properties, we also find that magnitudes/colours are affected by the completeness of the model atom employed for the calculations. Model s15e12iso is identical in ejecta structure to that of model s15e12 (same radius/velocity/density/temperature distribution), but differs in composition due to the treatment of underabundant species, ignored in model s15e12. We find stronger line blanketing in simulations based on model s15e12iso at the recombination epoch, in particular associated with the treatment of Sc II, Cr II, Fe I and Ni II, which leads to a reduction of the already faint *UB*-band magnitudes by $\lesssim$0.5 mag. As already realized for the modelling of SN1987A (Dessart & Hillier 2010), including all species, and in particular all underabundant intermediate-mass-elements/metals up to Fe/Co/Ni, and as many ionization stages as possible is critical for obtaining converged results. In SNe II modelling, however, it is not critical to include a huge number of levels, as we find that increasing the number of levels by a factor of a few from the choice given in Table 3 does not alter our results significantly.

6 SYNTHETIC SPECTRA

6.1 Global evolution

We now turn to a presentation of the synthetic spectra for our two simulations. Because the general spectroscopic evolution from the photospheric phase to the nebular phase is similar for both sequences, we show in Fig. 12 a montage for one simulation only, that based on model s15e12. Our continuous modelling is permitted by the treatment of the *entire* ejecta at all times. The inner-grid boundary is at the inner edge of the innermost ejecta shell; any material between that shell and the neutron star fell back and is thus not part of the ejecta by definition. In the full solution of the radiative transfer with CMFGEN, we adopt two inner-boundary types. The inner boundary is treated as diffusive (with an imposed inner-boundary luminosity of $L_{\odot}/10^6$) as long as the base optical depth is greater than $\sim$10. Afterwards, we switch to a zero-flux nebular-like inner-boundary. For the computation of spectra, we assume a hollow core. With such a full-ejecta approach, we can continuously model the ejecta as they evolve from optically thick to optically thin.

Fig. 12 shows the evolution of a spectral energy distribution that initially resembles that of a thermal emitter, with a decreasing continuum flux at 100–150 d after explosion when the ejecta become optically thin. As time progresses in the nebular phase, the P-Cygni profile morphology of lines transitions to that of pure emission, with a box-like structure typical of optically thin line formation from a hollow region expanding at near-constant speed (Castor 1970). Simultaneously, the continuum flux vanishes.

During the SN evolution, line features evolve considerably, reflecting the change in composition, ionization/temperature and density. At early times, the photospheric layers are hot and ionized and H I Balmer lines and He I 5878 Å are present. As recombination sets in, line blanketing caused by once-ionized intermediate-mass elements and metal species appears at all wavelengths smaller than $\sim$5000 Å (Fig. 13). This entire photospheric-phase evolution takes place at essentially constant composition, so that these spectral changes are governed by ionization changes. As the SN progresses into the nebular phase, lines forming through recombination (following photoionization) weaken because of the fading radiation field, and in particular the quasi-absence of ionizing photons, either in the Lyman or in the Balmer continuum (in reality, this is exaggerated by our neglect of non-thermal ionization by high-energy electrons). In contrast, forbidden lines, which form at low density by radiative de-excitation of collisionally excited levels, strengthen on top of an ever-fading continuum. The two most important forbidden lines that appear in essentially all nebular-phase SNe II spectra are the doublets [O I] 6303–6363 Å and [Ca II] 7291–7323 Å.

6.2 Nebular phase

Due to their faintness, and unimportance for cosmological studies, there have been relatively few nebular studies of SN. The most extensive nebular studies are for SN1987A. For example, Xu, Ross & McCray (1991) studied the Comptonization of gamma rays by cold electrons; Xu & McCray (1991) studied how non-thermal electrons are produced and downgraded; Xu et al. (1992) studied the formation of the H I lines; Li & McCray (1995) studied the formation of the He I emission lines; while Li & McCray (1993, 1995) studied the formation of the Ca II emission lines. Additional extensive studies of the nebular phase in SN1987A are by Kozma & Fransson (1998a,b) who discussed in detail the temperature and ionization structure, and the formation of the most important emission lines. A major result of the above studies is the need for mixing of hydrogen down to 700 km s^{-1}, with oxygen and helium present at even lower velocities. Kozma & Fransson (1998b) analysed the O I lines in SN1987A and found that the bulk of the oxygen was located between 400 and 2000 km s^{-1}, a result in broad agreement with the earlier studies of Li & McCray (1992).

During the nebular phase the continuum is optically thin and line formation is simplified. Line profiles during the nebular phase provide information about the distribution of material as a function of velocity, and its geometrical distribution. For example, an isolated emission line arising from a spherical hollow shell will exhibit a flat top, with its minimum width determined by the velocity at the inner edge of the shell (e.g. McCray 1993). As the Sobolev escape probability is independent of angle in a Hubble flow (see expressions of Castor 1970), this result holds independent of the line's optical depth (neglecting continuum absorption).

During the nebular phase, one probes the entire optically thin ejecta, although emission is biased towards the denser/slower/hotter inner regions where unstable isotopes are naturally more abundant. This inner region contains few tens of per cent of the total ejecta mass, and $\lesssim$10 per cent of the total ejecta kinetic energy in our models (Fig. 1). The faintness of all SNe at such epochs makes them difficult to observe at late times. However, because the nebular phase reveals the core of SNe II-P progenitors, it is a key source of information on the explosion, as well as the core properties of the progenitor star. Despite this importance, nebular-phase spectra of SNe II-P are scarce and thus not much has been extracted yet from this important phase (Dessart et al. 2010a). Dedicated campaigns to secure nebular spectra of SNe II-P are needed to improve upon this matter.

We show in Fig. 14 the optical and near-IR synthetic spectra obtained for the simulation based on the model s15e12 at 302 and 1040 d after explosion. While the black curve gives the full spectrum, coloured curves give the bound–bound contributions from individual species. At such late times, not only ^{56}Ni, but also ^{56}Co, have decayed and the metal mixture is dominated by ^{56}Fe. At 302 d, the synthetic spectrum is dominated by a forest of Ti II and Fe II lines in the region bluewards of 5500 Å. Further to the red, fewer Fe II lines are present (though in the simulation based on model s15e12iso, lines of Fe I are predicted), and three main features dominate the spectral landscape, the forbidden doublet lines of [O I] 6303–6363 Å and [Ca II] 7291–7323 Å, and the Ca II triplet at 8498, 8542, 8662 Å.

Downloaded from https://academic.oup.com/mnras/article/410/3/1739/962985 by CNRS - ISTO user on 30 November 2021

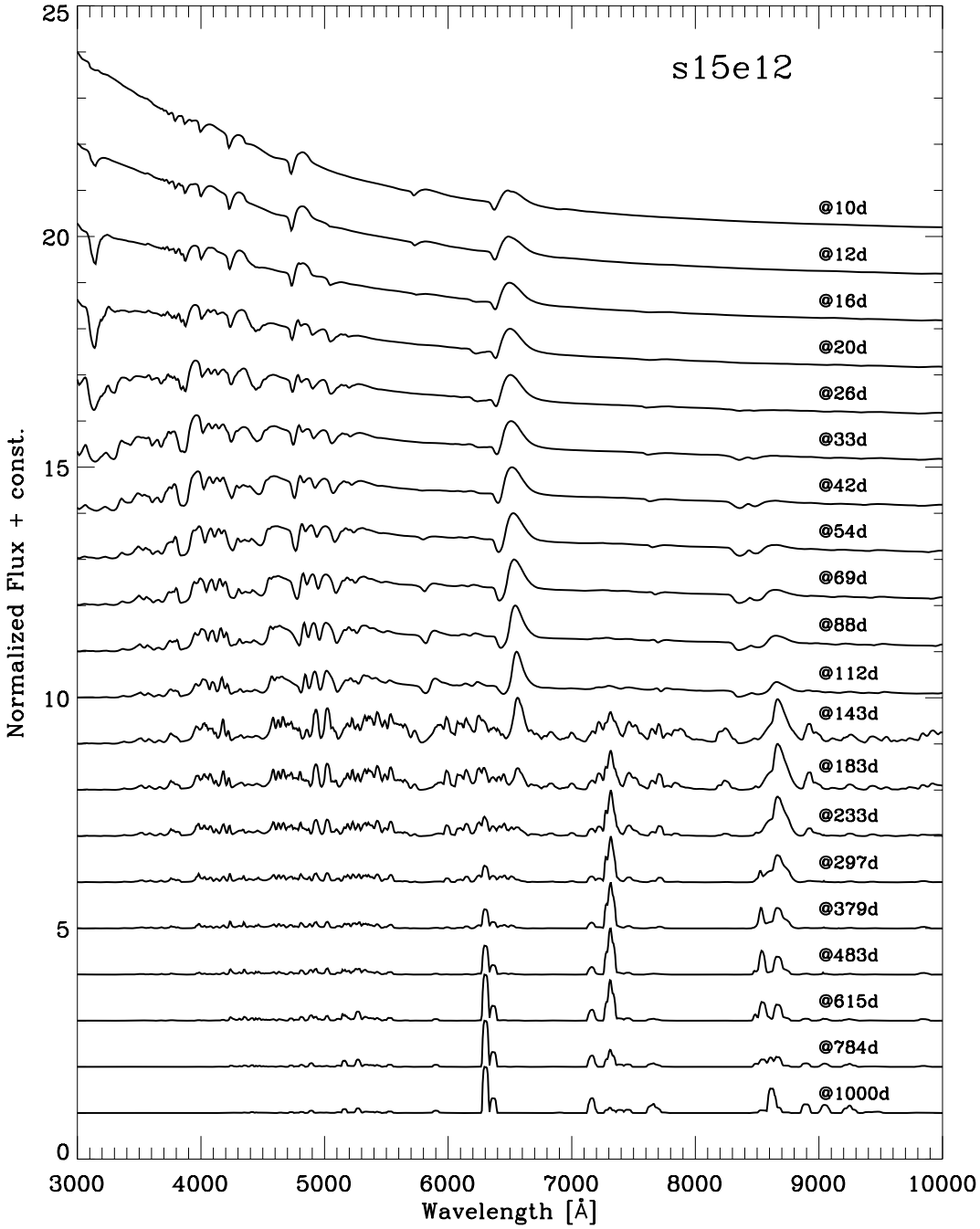

Figure 12. Montage of synthetic optical spectra covering epochs between 10 and 1000 d after explosion for our simulation based on model s15e12. The selected times, indicated by the label on the right, are such that the time interval between two consecutive spectra is constant in the log. For better visibility, each spectrum is first normalized to the peak flux in the region 6000-8000 Å, which introduces a variable scaling between epochs, and then shifted vertically for better visibility. During the photospheric phase, lines features are associated with H I Balmer lines, resonance lines like the triplet of Ca II at ∼8500 Å and forests of metals lines (e.g. Fe II and Ti II) causing severe line blanketing at wavelengths smaller than ∼5000 Å. During the nebular phase, forbidden lines like [O I] 6303–6363 Å and [Ca II] 7291–7323 Å progressively strengthen relative to recombination lines and the fading continuum.

As time proceeds, the decreasing ejecta electron/ion density favours the forbidden and 'resonance' transitions and so the features associated with [O I], [Ca II] and Ca II strengthen while the recombination transitions associated with Fe II weaken in the region 4000–5500 Å. At very late times, only [O I] and [Fe II] persist.

In our simulations we do not predict H I Balmer-line emission at nebular times. The Balmer lines fade abruptly when the ejecta become optically thin, immediately at the end of the plateau phase, a result of the sudden disappearance of Balmer-continuum photons and the de-excitation of H I. The treatment of non-thermal ionization/excitation would counteract the fading of the H I Balmer recombination lines at the end of the plateau phase, since it is precisely at that time that high-energy electrons can impact level populations and the ionization state of the gas in SNe II (Kozma & Fransson 1992, 1998a,b). We suspect this neglect is less critical for forbidden lines which form through transitions between levels that have a low excitation potential, and hence can be excited by thermal electrons.

© 2010 The Authors, MNRAS **410,** 1739–1760
Monthly Notices of the Royal Astronomical Society © 2010 RAS

Downloaded from https://academic.oup.com/mnras/article/410/3/1739/962985 by CNRS - ISTO user on 30 November 2021

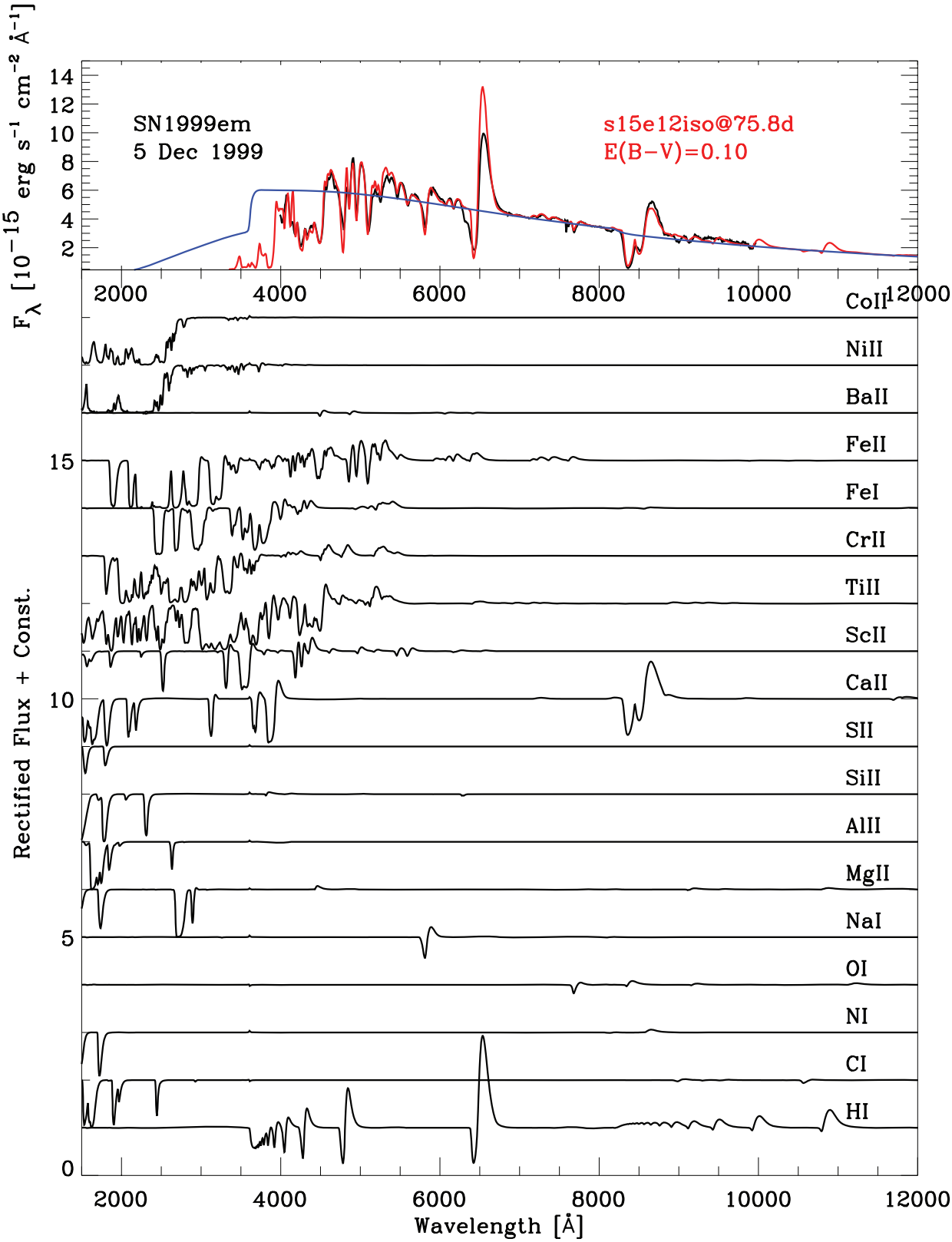

Figure 13. Illustration showing bound–bound contributions of selected species (bottom; fluxes are normalized to the continuum and shifted vertically) to the full synthetic spectrum (red curve, top panel) obtained in the simulation based on model s15e12iso at a post-explosion time of 75.8 d. The full and continuum-only (blue curve) synthetic spectra have been reddened [$E(B-V) = 0.1$] and distance scaled ($D = 11.5$ Mpc; an additional scaling by a factor of 2.3 is added to compensate for the higher brightness of the model), and in the top panel are compared for illustration to the Keck observations of SN1999em on 1999 Dec. 5 (black; Leonard et al. 2002)

Downloaded from https://academic.oup.com/mnras/article/410/3/1739/962985 by CNRS - ISTO user on 30 November 2021

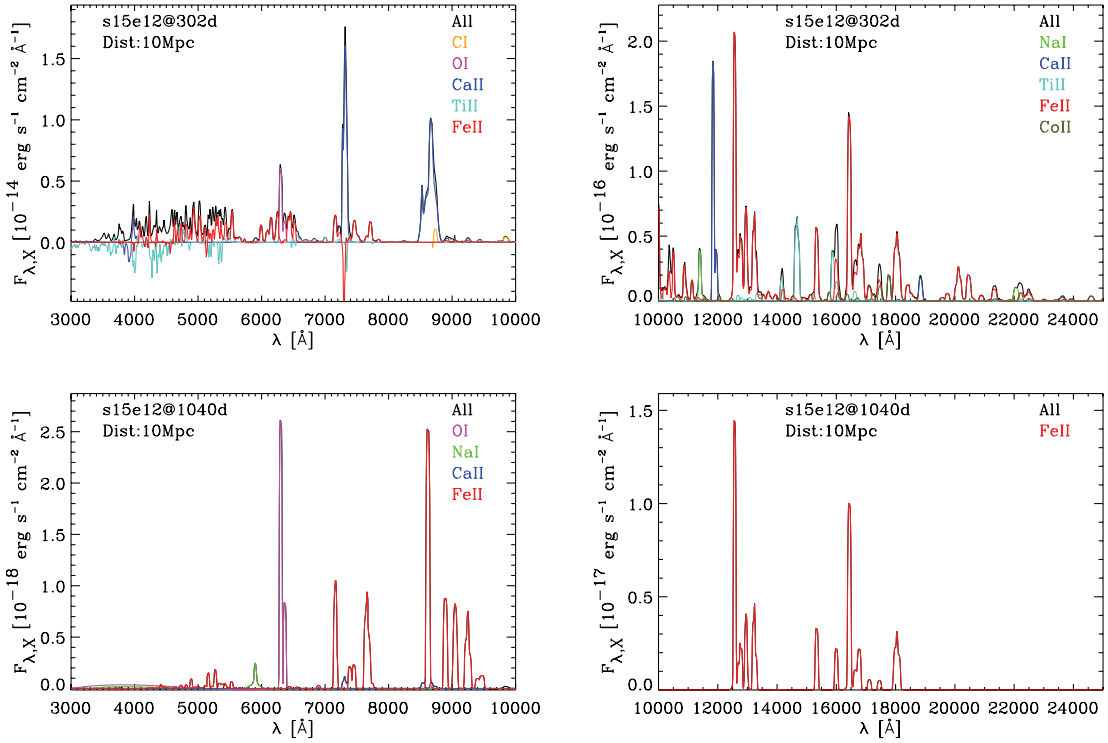

Figure 14. Illustration of optical (left-hand column) and near-IR (right-hand column) synthetic spectra obtained for the simulation based on model s15e12 at post-explosion times of 302 d (top row) and 1040 d (bottom row). The full synthetic spectrum is shown as a black curve, while overplotted coloured lines refer to the flux obtained when including bound–bound transitions exclusively of the species labelled on the right of each panel. We only display the results for those species that matter to the emergent flux, hence the selection varies between panels (i.e. for different times and spectral ranges). At late times, only forbidden lines, forming in the inner SN-ejecta regions corresponding to the former progenitor helium core, contribute to the SN light. The continuum flux is a few orders of magnitude smaller than the full synthetic flux due to lines.

The rapid disappearance of the H I lines at the end of the plateau phase indicates that non-thermal processes must be crucial for the hydrogen ionization, even at ∼150 d. This is in apparent contradiction with the conclusions of Kozma & Fransson (1998b) who indicate that in SN1987A, H ionization is determined by photoionization from the $n = 2$ level up to 500 d. A likely explanation is that non-thermal excitation from the ground state, together with the large optical depth of Lyα, helps to maintain (set) the $n = 2$ population from which ionization occurs. The viability of this option can be verified by solving the two-level atom plus continuum problem (see e.g. equation 39 of Kozma & Fransson 1992).

In model s15e12, and at a representative post-explosion time of 332 d, we find that the doublet lines [O I] 6303–6363 Å and [Ca II] 7291–7323 Å form primarily in the inner denser ejecta. This is illustrated by the similar and relatively modest broadening, of Doppler origin, of the corresponding individual line components. Indeed, the full width at half-maximum of ∼2500 km s^{-1} corresponds quite closely to the velocity of ∼1500 km s^{-1} of the outer helium-core (see Fig. 1, but also Fig. 2).

In contrast, the strong permitted transitions of Ca II at 8498, 8542, 8662 Å show a hybrid formation, with contributions from both the inner and outer ejecta. This gives a very peculiar shape to the Ca II 8662 Å line, with a relatively narrow emission part associated with the ejecta region corresponding to the progenitor helium-core, and a broad emission part associated with the hydrogen-rich region of the SN ejecta (Fig. 15). The second, broad, component suggests that emission comes from the entire volume of the ejecta, all the way to the outermost mass shells (see Fig. 1). Excluding Ca II 8662 Å line (discussed below), simulated emission line profiles show that the bulk of their emission at nebular times comes from the same region of space, which corresponds to the progenitor helium core.

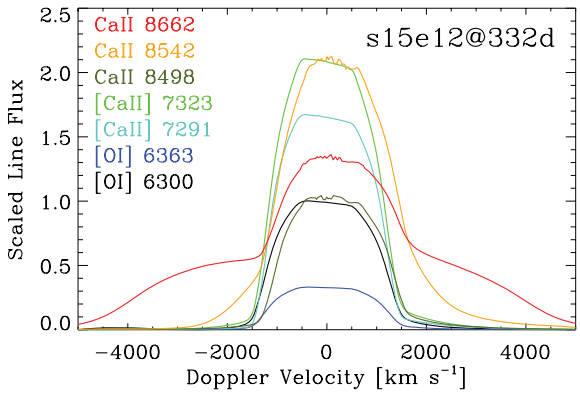

Figure 15. Illustration of the synthetic line flux for the simulation based on model s15e12 at 332 d after explosion, and associated with individual transitions giving rise to the forbidden lines of [O I] and [Ca II], as well as the 'resonance' transitions of Ca II appearing around 8500 Å. All fluxes are normalized to the peak flux of the O I 6303 line. A colour coding is used to differentiate individual line transitions. Notice the similar and relatively narrow width of most of these lines, reflecting the expansion speed of the helium-core in which they form, while resonance transitions of Ca II form not only in that same inner region, but also in the outer hydrogen-rich ejecta. Individual profiles were computed ignoring interactions with overlapping lines.

The Grotrian diagram for Ca II is rather simple and it is not initially obvious why Ca II 8662 Å should show such a different line profile

Downloaded from https://academic.oup.com/mnras/article/410/3/1739/962985 by CNRS - ISTO user on 30 November 2021

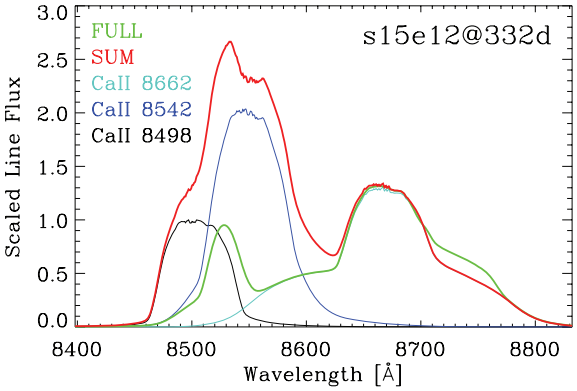

Figure 16. A comparison of the theoretical spectrum in the neighbourhood of the Ca II triplet ('FULL'; green), and that obtained by summing line profiles for individual members of the triplet ('SUM'; red). Individual components are drawn as thin coloured lines. The 'summed' spectrum is very different from the true spectrum, particularly for the 8498 and 8542 Å lines which contain too much flux in the 'summed' spectrum. As explained in the text, photons in 8498 and 8542 Å are absorbed and re-emitted in the 8662 Å line.

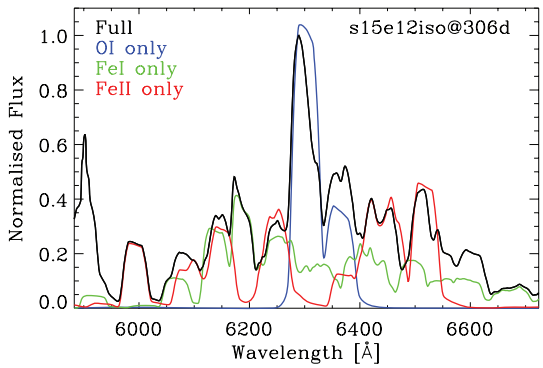

Figure 17. Full synthetic spectrum (black) for model s15e12iso at 306 d after explosion and showing the [O I] 6303–6363 Å region. To illustrate the presence of line overlap, we overplot the synthetic spectrum obtained by accounting for bound–bound transitions of O I (blue), Fe I (green) or Fe II (red) exclusively. Line overlap and associated line-optical depth effects compromise any eye-ball estimate of the flux contribution associated with O I.

from the other lines. A hint comes from comparing the Ca II triplet spectrum to that obtained by summing the individual profiles. As shown in Fig. 16, there is a lot more flux in the two bluest lines than in the full spectrum. This suggests that the photons emitted in Ca II at 8498 and 8542 are scattered in the Ca II 8662 Å elsewhere in the envelope. This is reasonable since the triplet transitions are optically thick, and the velocity shift between neighbouring lines is only $\sim$1500 km s^{-1} and $\sim$4200 km s^{-1}. Examination of the Ca II triplet profile on day 198 for SN1987A also shows a complex profile, with the 8662 Å line being much broader than the 8498/8542 Å blend (Phillips et al. 1990; Li & McCray 1993).

Our theoretical spectra also reveal a wealth of weak emission lines which blend with many of the stronger features. This was previously highlighted by Kozma & Fransson (1998b) for O I. They noted that the ratio of O λ6300 to λ6363 was significantly less than the theoretical value of 3., which they attribute to a blend of Fe I 6361 Å. In our calculations, we find that this [O I] region overlaps with numerous Fe I and Fe II lines (Fig. 17), and thus may complicate the determination of the oxygen-mass ejected (Dessart et al. 2010a).

6.3 Comparison between simulations based on the s15 and s25 models

We have so far focused on the spectroscopic properties obtained for one time sequence. We now compare the spectroscopic differences between the simulations based on models s15e12 and s25e12, which both have the same explosion energy, were evolved under the same conditions (no rotation, solar-metallicity environment), but started from stars with main-sequence masses of 15 and 25 M$_\odot$. In Section 2, we discussed the key differences between the two pre-SN stars, which are the larger progenitor radius in model s25e12, the more pronounced He/N enhancement in the envelope of model s25e12 and the larger helium-core mass in model s25e12. Indeed, model s25e12 ejects 6.29 M$_\odot$ of helium-core embedded material, while s15e12 ejects only 2.44 M$_\odot$. Here, we discuss the radiative signatures resulting from such differences in progenitor and explosion properties. We show comparative spectra for the two simulations at the same post-explosion time during the photospheric and nebular phases in Fig. 18.

As discussed above, the larger progenitor radius for a given explosion energy gives bluer colours and a brighter bolometric display (larger flux) during the plateau phase, while the large ^{56}Ni yields in model s25e12 give a higher nebular luminosity (at a given post-explosion time). During the recombination epoch, when the simulations show similar colours, contemporaneous spectra obtained for the two simulations show a remarkable similarity. The difference in composition, imprinted in H/He/C/N/O, is largely masked and photospheric-phase spectroscopy is unable to lift this apparent degeneracy. The few C I, N I and O I lines appearing in the red part of the optical are too weak to allow a reliable and meaningful assessment of CNO abundances. After about 15 d after explosion, He I lines disappear, and the weak sensitivity of the H I Balmer lines to the H/He abundance ratio compromises even this determination.

Quite paradoxically, most inferences on SNe II-P are based on observations during the photospheric phase, which, as we have illustrated here, boasts very degenerate properties that prevent a clear assessment of the progenitor properties. Having recourse to nebular-phase spectra can help lift this degeneracy in a number of ways. Because the helium-core mass increases with main-sequence mass, the relative fraction of the ejecta that it represents grows with main-sequence mass. Dessart et al. (2010a) demonstrated that for a given explosion energy, the ejection velocity of core-embedded oxygen-rich material is an increasing function of main-sequence mass. The width of [O I] 6303–6363 Å can be used as a diagnostic of this differential expansion speed. Its strength can then be used to constrain the total amount of core-embedded oxygen ejected. Together with the constraint on the helium-core mass (which is set by the main-sequence mass), one may have a means to constrain the mass of the compact remnant formed.

We plan a forthcoming parameter study using non-LTE time-dependent simulations based on models of SNe II-P with different main-sequence mass, explosion energies and ^{56}Ni. This will reveal a wealth of information, and document what SNe II-P ejecta properties condition the [O I] strength and width. Based on the two simulations presented here, we find that the doublet line [O I] 6303–6363 Å is both broader and stronger in the simulation based on the higher-mass progenitor, and this results from differences in the pre-SN stars rather than in the explosion properties (Fig. 19; note that the enforcement of homology alters somewhat the inner-ejecta kinematics). The $\sim$30 per cent larger core-embedded oxygen ejection speed in model s25e12 is reflected by the greater width of each component of the [O I] doublet line, while the larger

Downloaded from https://academic.oup.com/mnras/article/410/3/1739/962985 by CNRS - ISTO user on 30 November 2021

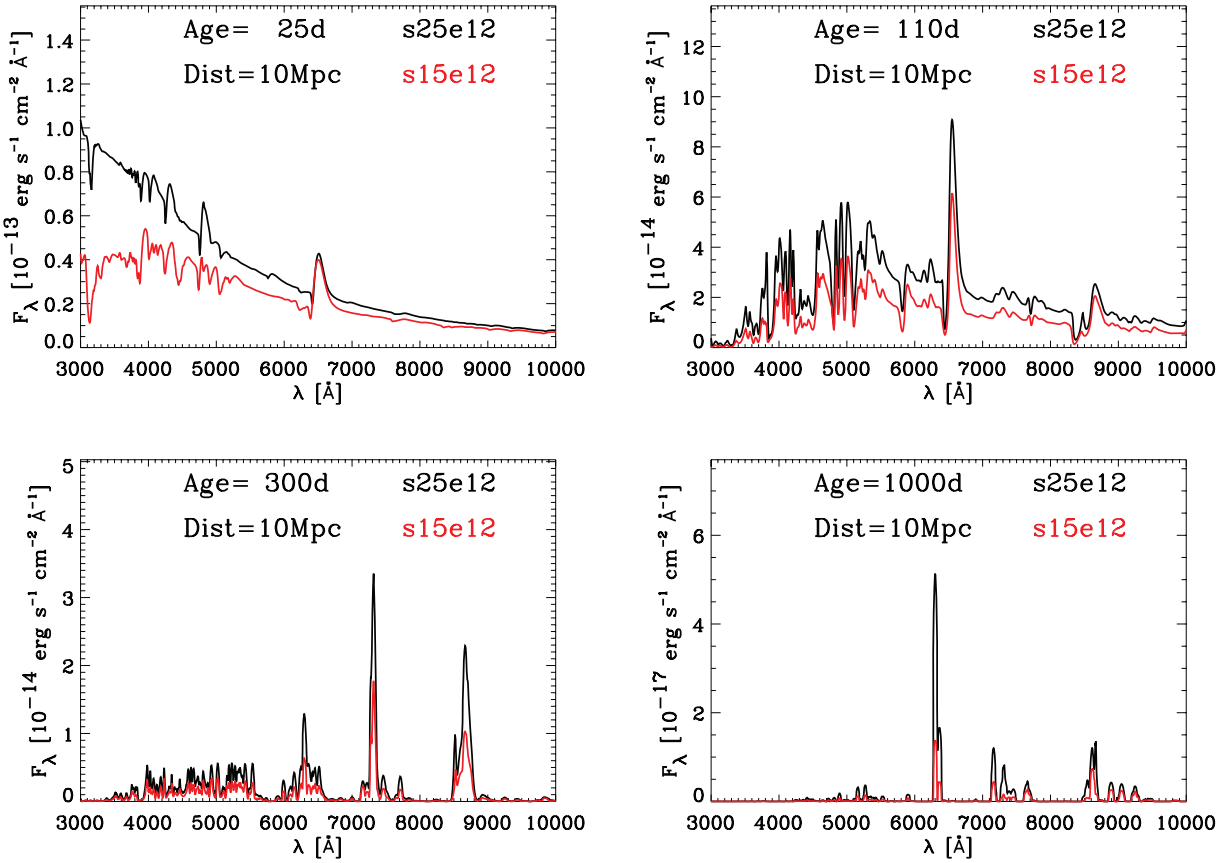

Figure 18. Comparison between optical synthetic spectra for the simulations based on model s15e12 (red) and s25e12 (black) and shown at post-explosion times of 25 d (top left), 110 d (top right), 300 d (bottom left) and 1000 d (bottom right). Only a distance scaling is performed on these synthetic spectra, adopting a value of 10 Mpc.

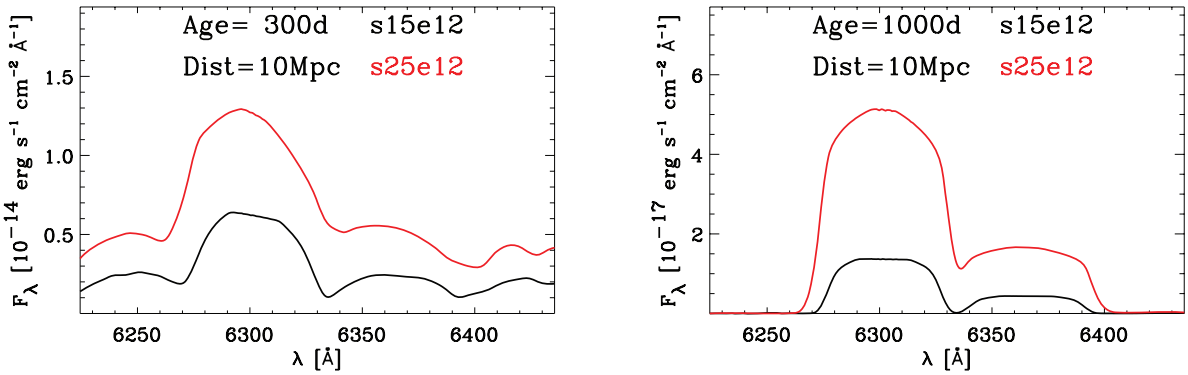

Figure 19. Same as Fig. 18, but now showing the [O I] 6303–6363Å doublet region at 300 d (left) and 1000 d (right).

core-embedded oxygen ejected mass in model s25e12 (3.32 compared to 0.816 $M_\odot$) is reflected by the higher line flux at all nebular epochs (this is also influenced by the ^{56}Ni mass). Clumping and subtleties associated with radioactive heating will complicate a quantitative assessment here, but this differential reasoning at least opens a route towards constraining in a systematic fashion the properties of the inner ejecta of SNe II-P.

6.4 Comparison between simulations based on s15e12 and s15e12iso models

As detailed previously in Section 2, models s15e12 and s15e12iso differ in their composition, and our simulations based on these simulations reflect that distinction, as well as the additional treatment of ions in the model atom (see Table 3). In our simulation based on model s15e12, we also neglected some species for which no associated line feature was ever seen, such as neon or argon. In that case, we applied a scaling on the rest of the elements to normalize the sum of mass fractions to unity – this scaling modifies by ∼10 per cent the abundances in the helium core. The difference in composition between the two models contains two components. First, some species are included in model s15e12iso, like Sc or Ba, which are missing in model s15e12. Secondly, model s15e12iso gives the distribution of species versus depth. It shows, for example, an increase in sodium abundance towards the core, while in model s15e12 sodium is taken at its solar-metallicity value.

Downloaded from https://academic.oup.com/mnras/article/410/3/1739/962985 by CNRS - ISTO user on 30 November 2021

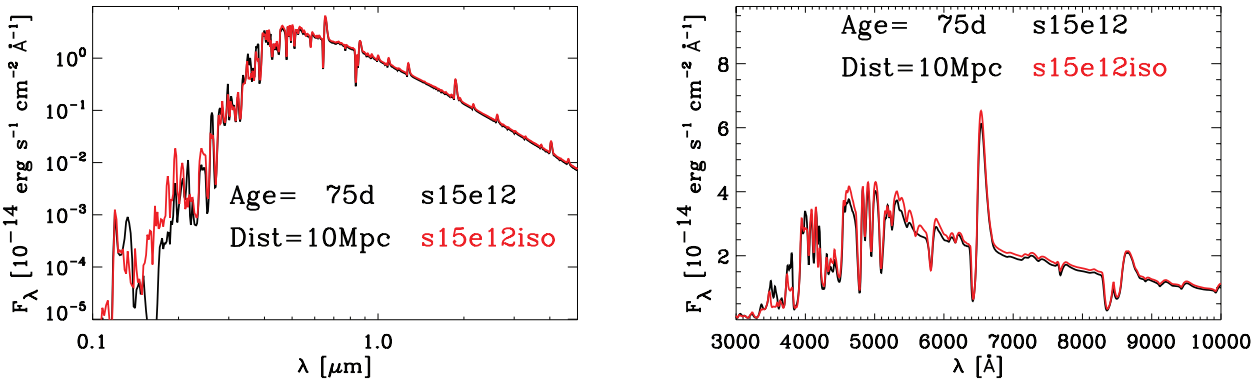

Figure 20. Left: Log–log plot showing synthetic spectra at 75 d (41st time-step in the sequence for each) after explosion for the simulations based on models s15e12 (black) and s15e12iso (red). The spectral range covers from 1000 Å to 5 μm. Right: same as left, but now showing the optical range only and using a linear scale.

So, when comparing synthetic spectra from our simulations based on models s15e12 and s15e12iso, both composition and model atom differences intervene. We show in Fig. 20 the differences at the same post-explosion time of 75 d for each simulation. There is ∼5 per cent absolute flux level difference between the two, with significant differences appearing in the UV, and essentially none beyond $\lesssim$1 μm. The enhanced UV flux in the simulations based on model s15e12iso may stem from the reduced metal abundances, in favour of the treatment of species like Ar or Ne which have little blocking power, while the reduced *UB*-band flux is caused by the treatment of additional blanketing sources (e.g. Fe I or Ni II; see Fig. 13 for an illustration of individual contributions). Lines of Sc II, whose abundance is zero in model s15e12, are predicted in the simulation based on model s15e12iso. Similarly, the Na I D doublet line is stronger in that simulation, which reflects the increasing sodium mass fraction in model s15e12iso with depth. During the nebular phase, differences are significant between the two simulations (not shown), but they are primarily associated with the treatment of Fe I.

Although the spectral evolution computed for simulations based on models s15e12 and s15e12iso is essentially the same, the model with a more complete set of metals and model atom yields stronger line blanketing (which translates into a weaker flux in the *UB* bands) as well as the prediction of specific lines associated with, for example, Sc II (Fig. 13).

7 COMPARISON WITH OBSERVATIONS

7.1 Bolometric luminosity and light curves

Observed *V*-band light curves of a large sample of SNe II-P have been presented in Hamuy (2003) or Poznanski et al. (2009). These suggest that despite the expected variations in progenitor (Levesque et al. 2005) and explosion properties (Burrows et al. 2007a,b; Marek & Janka 2009), their properties are quite uniform (those wishing to standardize such SNe for distance determinations will find instead that there is a sizeable scatter). Quite generally, about 10–20 d after the inferred time of explosion, the visual brightness levels off or fades slowly (corresponding to a typical luminosity of $\sim 1.2 \times 10^{42}$ erg). When reaching 75–120 d after explosion, the SN fades by 0.8–1.2 dex in luminosity as it transitions on a time-scale of a few weeks from the plateau phase to the nebular phase (Bersten & Hamuy 2009).

Our simulations reveal plateau-phase bolometric luminosities (Fig. 9) that are a factor of 2 too large compared to observations. Indeed, the absolute *V*-band light curves we obtain are brighter than those we derived from detailed modelling of SNe 1999em and 2006bp (Dessart & Hillier 2006; Dessart et al. 2008). To illustrate this discrepancy, we show a comparison of our reddened and distance-scaled synthetic light curves to observations of SN1999em (Leonard et al. 2002) in Fig. 21. Interestingly, the same discrepancy applies to the simulations of SNe II-P light curves presented in Kasen & Woosley (2009). In contrast, the simulation of Eastman et al. (1994), which is based on a 15 $M_\odot$ progenitor star characterized by a smaller radius of 480 $R_\odot$, predicts a representative plateau-phase bolometric luminosity of $\sim 4 \times 10^8$ $L_\odot$ and a peak *V*-band magnitude of about −17. Hence, we surmise that the main problem with the progenitors used in recent SNe II-P simulations (including this work) is the progenitor radius, which is systematically too large, and perhaps the helium mass fraction in the hydrogen envelope, which is too low.

Our simulations have an explosion energy of 1.2 B and a ^{56}Ni mass that may not fit specific SNe II-P but is representative of the standard and thus should not be the cause of this overall discrepancy. Finally, in the simulations of SN1987A performed with the same code (Dessart & Hillier 2010), we did reproduce the observed SN1987A light curve to within 10 per cent in flux at all times between 0.3 and 21 d. This agreement suggests there is a physical discrepancy with the pre-SN RSG stars we employ at present. We speculate that RSG progenitors with a surface radius intermediate between the blue-supergiant progenitor of SN1987A (∼50 $R_\odot$) and those of the RSG progenitors of models s15e12/s25e12 (810/1350 $R_\odot$) would correspondingly reveal light curves that are intermediate between those produced from our simulations of SN1987A and those from models s15e12/s25e12.

A faster increase in (or a globally larger) helium mass fraction in the hydrogen-rich envelope would likely remedy the sustained visual brightening obtained with our models during the plateau phase. Indeed, in this context, the progression of the recombination wave is faster, leading to a faster decline of the photospheric radius than presently predicted (Fig. 4). In our non-LTE steady-state simulations for SNe 2005cs and 2006bp (Dessart et al. 2008), we employed a chemical mixture with depleted H/C/O and enhanced He/N (a similar trend was obtained by Baron et al. 2007), resembling closely the surface composition of model s25e12, but not that of model s15e12. As discussed earlier, there is evidence of mixing in RSG stars which points in this direction of enhanced He/N (Lançon et al. 2007), perhaps as a result of stellar rotation. This determination of

Downloaded from https://academic.oup.com/mnras/article/410/3/1739/962985 by CNRS - ISTO user on 30 November 2021

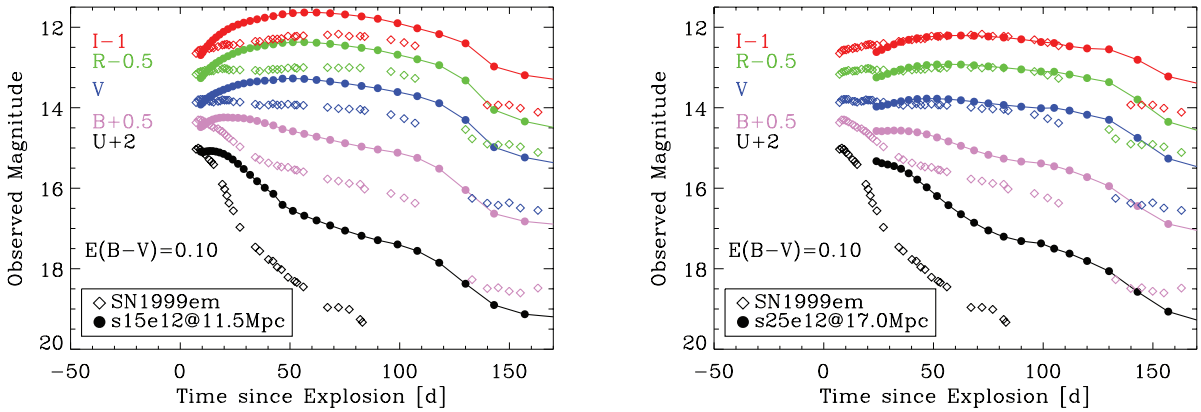

Figure 21. Left: comparison between the observed multi-colour light-curve (diamonds) of SN1999em (Leonard et al. 2002) and the corresponding reddened [$E(B-V) = 0.1$] and distance scaled ($D = 11.5$ Mpc; Dessart & Hillier 2006) magnitudes from the s15e12 model (dots). A further vertical shift is applied to avoid overlap, as in Leonard et al. (2002). Note the excellent agreement at day 9 for each band (see spectral comparison at that epoch in Fig. 22), but the subsequent divergence between observed and synthetic magnitudes. This suggests a significant mismatch between the structure of the RSG progenitor model and/or explosion energy with that corresponding to the progenitor of 99em. This may stem from the mismatch in density distribution, which is in evidence in Fig. 22. Right: same as left, but now for the time sequence based on model s25e12 (we now scale the synthetic magnitudes adopting an SN distance of 17 Mpc).

H/He/C/N/O abundances is best done with early-time observations of SNe II-P, when the photospheric layers are fully or partially ionized. This issue is important to resolve, as it has ramifications both for the modelling of SN light and for the understanding of mixing processes in massive stars prior to the explosion.

As in our simulations of SN1987A, there are residual problems with the UV range and *UB* bands. The flux that falls within these regions is typically smaller, or much smaller, than the visual flux. This region is strongly affected by line blanketing, which effectively absorbs the relatively small flux appearing bluewards of $\lesssim$4000 Å at the thermalization depth. This line blanketing is caused by underabundant metal species, and may also be affected by the floor temperature we employ in our simulations. For example, the additional contributions from Sc II, Cr II, Fe I and Ni II in simulations based on model s15e12iso led to a steeper decline and $\lesssim$0.5 mag-fainter *UB*-band magnitudes than obtained with model s15e12. This sensitivity suggests that the discrepancy is really connected to completeness of the model atoms, although tests have not revealed any obvious candidate species, or a problem with the adopted model atoms. As we neglect many neutral species we will underestimate the line blanketing, particularly at late time. Examination of the *U*-band light curve presented by Kasen & Woosley (2009) for their standard II-P model shows less of a discrepancy with the $U - V$ colour, further hinting to a possible problem with our adopted atomic data.

The metallicity at the site of the explosion could also play a role (it may not be solar, as assumed here), as could the H/He abundance ratio. The H/He abundance ratio modifies the way radiation thermalizes so that for enhanced helium abundance, the UV flux drops. A higher helium mass fraction in the hydrogen-envelope of the RSG progenitors would thus lead to a faster visual-brightness decline and a fainter UV flux, both improving the match to standard observations of SNe II-P.

7.2 Photospheric- and nebular-phase spectra

As described above, the absolute brightness and spectral evolution predicted with the simulations performed in this paper differ quantitatively from that of standard SNe II-P. However, modulo an absolute scaling to get the fluxes in correspondence, and allowing for an adjustment in time, we can compare our synthetic spectra to individual observations. Here, we use the spectroscopic observations of SN1999em, for which we also have tailored simulations computed with a steady-state approach (Dessart & Hillier 2006).

Our simulation at 9.3 d and based on model s15e12iso matches the SN1999em observations on 1999 November 3 (Hamuy et al. 2001) both in relative and in absolute flux in the optical (Fig. 22). Similarly, the equivalent steady-state model computed for that date (right-hand panel; Dessart & Hillier 2006) shows the same colour and reproduces the overall flux very well. However, the equivalent steady-state model reproduces line profile strengths much better. Time dependence might play a role here, but more likely, the mass-density profile in the outer ejecta of model s15e12iso is the culprit.

At very early post-explosion times, a density exponent of 15–50 is required to reproduce the observations of SNe 2005cs and 2006bp (Dessart et al. 2008), but at 10 d after explosion, this density exponent was found to be of the order of 10 in the photospheric region for these SNe, as well as for SN1999em (Dessart & Hillier 2006). In our simulations (s15e12/s15e12iso), the photosphere resides from day 10 to day 25 in the outer ejecta layers where the density exponent is approximately 25 (!). This then seems the most probable reason for the underestimated line strength (see the discussion of the effect of the density exponent on Balmer-line profile morphology in Dessart & Hillier 2005b). The progenitor star may have a different structure. For example, the density exponent for the corresponding regions (velocity in the range 7000–9000 km s^{-1}) in our 87A model ejecta, produced from the explosion of a 50 R$_\odot$ BSG star, is 8 (Dessart & Hillier 2010). Furthermore, simulations of SNe II-P ejecta tend to have low resolution in the outermost mass shells, which questions the accuracy of these layers and the corresponding early-time SN photospheric properties.

As the ejecta recombine and the photosphere recede into deeper layers, the line strengths increase. At such times, we reproduce the observations of SN1999em extremely well (upper two panels of Fig. 23). For the observations of SN1999em on 1999 December 5, we also illustrate the various bound–bound transitions that contribute to the observed line features in Fig. 13. We also include here a comparison of the nebular-phase spectrum of SN1999em taken on 2000 Sept. 26 (Leonard et al. 2002) with the synthetic spectrum at 306 d from our simulation based on model s15e12iso (synthetic

© 2010 The Authors, MNRAS **410,** 1739–1760
Monthly Notices of the Royal Astronomical Society © 2010 RAS

Downloaded from https://academic.oup.com/mnras/article/410/3/1739/962985 by CNRS - ISTO user on 30 November 2021

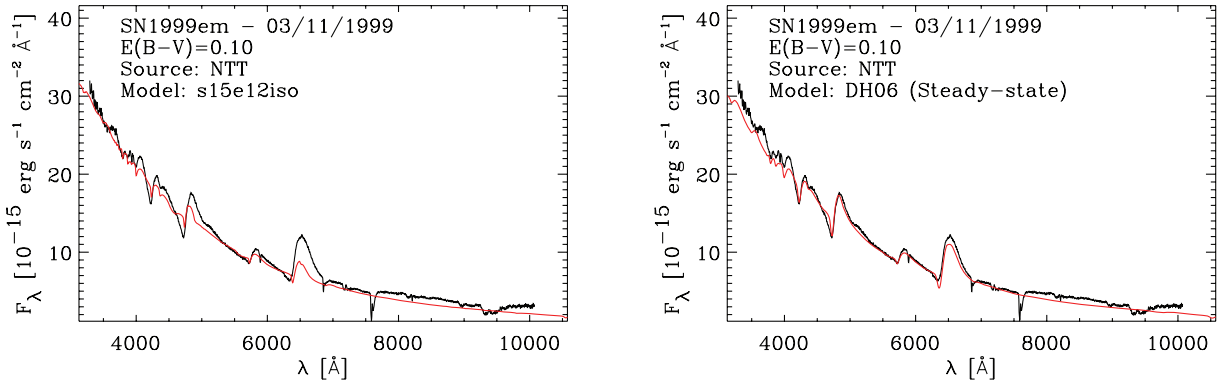

Figure 22. Left: comparison between the observations of SN1999em on the 1999 November 3 (Hamuy et al. 2001) with the reddened and distance-scaled synthetic spectrum obtained from the s15e12iso model on day 9.3 evolved with the time-dependent solver. Right: same as left, but now using the model of Dessart & Hillier (2006) for the same date, which is computed with a steady-state solver (which also accounts for v/c terms appearing in the radiative-transfer equation). The difference between the two models is caused by the steeper density distribution in the hydrodynamical input s15e12iso, corresponding to $N_\rho \sim 25$ in the photospheric region at the time, compared to $N_\rho = 10$ used in the steady-state calculation. This affects significantly the flux in recombination lines, as well as the evolution of the light curve and colours, and suggests that the hydro input is not fully adequate.

spectra are scaled to correct for the magnitude mismatch illustrated in Fig. 21). Recall that SN1999em is thought to have produced 0.036 $M_\odot$ of ^{56}Ni (Utrobin 2007) while model s15e12iso contains initially 0.086 $M_\odot$. The agreement is good, especially since no parameter is adjusted in model s15e12iso to match the observations. The only, and sizeable, discrepancy is the complete absence of Hα in our synthetic spectrum, while a strong flux is observed instead. We also note that we predict a sudden disappearance of the continuum flux at the end of the plateau phase, while observations suggest a more gradual fading of the continuum flux relative to lines. Such discrepancies stem entirely from our neglect of non-thermal excitation/ionization. Remarkably, it may be that this additional process does not affect other species much.[5] In any case, this physical ingredient is essential for quantitative modelling of the nebular phase of SNe II and will be incorporated in CMFGEN in the near future.

8 DISCUSSION AND CONCLUSIONS

We have presented the first non-LTE time-dependent radiative-transfer simulations of SNe II-P covering from the early photospheric phase until $\gtrsim$1000 d after explosion. Our simulations start from hydrodynamical models of the explosion of two RSG stars, evolved from non-rotating solar-metallicity stars with main-sequence masses of 15 and 25 $M_\odot$. The main assets of our approach are (1) the treatment of non-LTE for all level populations, (2) the explicit treatment of line-blanketing, (3) the consideration of all time-dependent terms appearing in the statistical-equilibrium, energy and radiative-transfer equations, (4) the adoption of a hydrodynamical model describing the density/temperature/radius/velocity distribution as well as the complex chemical stratification in the SN ejecta and (5) the modelling of the *entire* ejecta at all times. The main approximations of our approach are spherical symmetry, homologous expansion and the treatment of radioactive decay as a local heating source (thus ignoring the effects of non-thermal excitation and ionization).

[5] Non-thermal processes will likely increase the electron density but this will only have a secondary effect on many of the lines since they are the coolants, and hence their strength is primarily determined by energy deposition from radioactive decay.

From our simulations, we find/infer the following.

(i) The photospheric evolution during the plateau phase shows a continuous radius increase up to 2.5–3 $\times$ 10^{15} cm at $\sim$80 d, a decrease and then a plateau in temperature at $\sim$5000 K and a continuous decrease in velocity as the ejecta optical thickness diminishes with expansion and recombination. This is in qualitative agreement with that inferred from observation, and is similar to the trend we obtained for SN1987A (Dessart & Hillier 2010).

(ii) The synthetic bolometric luminosity shows a very gradual decline (not quite a plateau) during the photospheric phase. At 50 d after explosion our models have bolometric luminosities of $\sim 6 \times 10^8$ $L_\odot$ for model s15e12 and $\sim 10^9$ $L_\odot$ for model s25e12. These are a factor of 2 to 3 larger than the standard 50-d luminosity of $\sim 3 \times 10^8$ $L_\odot$ for observed SNe II-P (Bersten & Hamuy 2009). Similar overestimates result from the simulations of Kasen & Woosley (2009), which are based on similar progenitor models. However the simulation of Eastman et al. (1994), based on a more compact pre-SN RSG star, is in agreement with observations. This suggests that the pre-SN RSG stars produced by current stellar-evolutionary models have surface radii that are too large, on average.

(iii) The density distribution of the photosphere is too steep in our models, at 10 to 30 d after core collapse, yielding line strengths that are weaker than observed prior to the onset of the recombination phase. This may independently indicate that the progenitor surface radii are too large in our models. Steady-state models indicate that density exponents of $\sim$10 (i.e. $\rho \propto r^{-10}$) rather than $\sim$25 (valid at early times for the present models) are required to fit the line strengths.

(iv) At the end of the plateau phase, our computed bolometric luminosities decrease by a factor of a few over a time-scale of about a month until reaching a rate that corresponds to the instantaneous decay-energy production rate. In our simulations, the magnitude of the fading at the end of the photospheric phase is conditioned by two properties that are not obviously linked – the progenitor radius and the ^{56}Ni mass produced, and is thus expected to occur with a scatter in nature.

(v) Our multi-band light curves tend to show bell-shaped curves, with a peak that occurs earlier for filters positioned at shorter wavelength, and a width that increases for filters positioned at longer wavelength. This morphology is similar to that seen for SN1987A

Downloaded from https://academic.oup.com/mnras/article/410/3/1739/962985 by CNRS - ISTO user on 30 November 2021

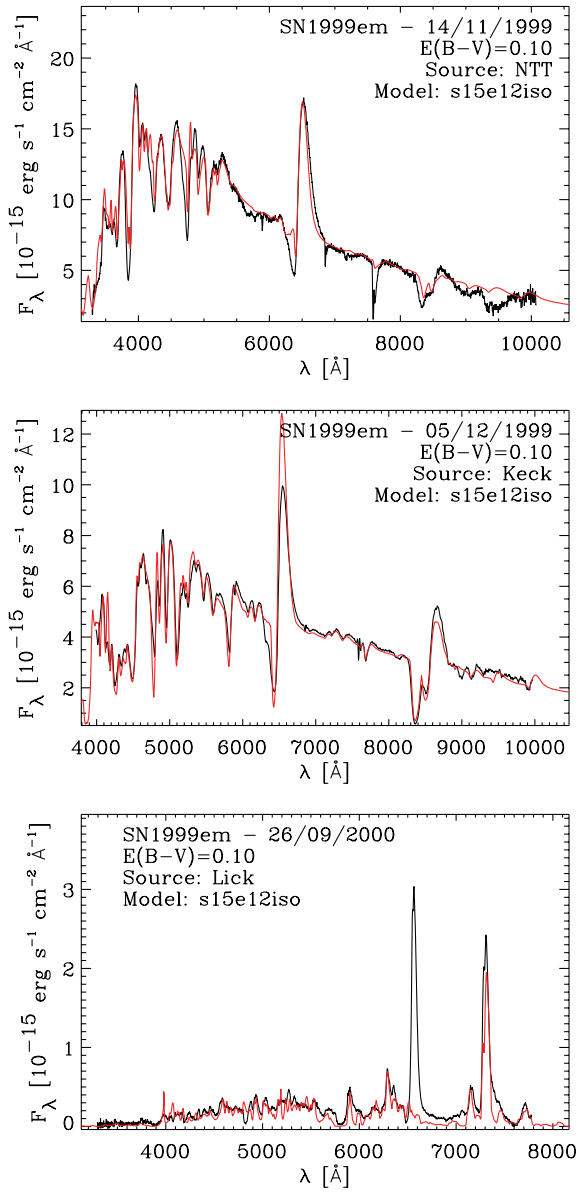

Figure 23. Top: comparison between the reddened synthetic spectrum from our simulations s15e12iso at a post-explosion time of 32.1 d with the New Technology Telescope (NTT) observations on 1999 Nov. 14 of SN1999em (Hamuy et al. 2001). This observation corresponds to an inferred post-explosion time of ∼22 d (Dessart & Hillier 2006). These dates do not match. Instead, our choice is done so that the observations and models have the same colour. Middle: same as top, but now for the s15e12iso at a post-explosion time of 75.8 d and the Keck observations on 1999 Dec. 5 (Leonard et al. 2002), corresponding to a post-explosion time of 42 d. Bottom: same as top, but now for the model s15e12iso at a post-explosion time of 306 d and the Lick observations of 2000 September 26 (331 d after discovery). In each panel, the synthetic spectra have been scaled to correct for the magnitude mismatch shown in Fig. 21.

(Phillips et al. 1988; Dessart & Hillier 2010), but the larger RSG progenitors corresponding to our models cause the effective/colour temperature to decline more slowly (and the more so for model s25e12 because of its larger radius). Comparison with SN1999em (Leonard et al. 2002) confirms that decline in effective/colour temperature is too slow, with the *UB* magnitudes remaining large for about 10–20 d.

(vi) As for our simulations of SN1987A, we predict too strong UV and *U*-band fluxes during much of the photosphere phase. This is likely due to inadequate model atoms, or the H/He abundance ratio in the envelope, and is currently being investigated.

(vii) In both simulations, the photosphere resides in the outer 1 $M_\odot$ of the SN ejecta for ∼50 d after the explosion. Thus, spectra taken during this time do not reveal any information about the chemical and density structure of the bulk of the mass. The confinement of the photosphere to the outer layers also provides a simple explanation for the low linear-polarization measures of SNe II-P at early times (Leonard & Filippenko 2005; Leonard et al. 2006; Chornock et al. 2010), and the notion that early-time SNe II-P spectra are relatively unaffected by the details of the explosion (e.g. geometry and ^{56}Ni production). Rather, SNe II-P evolve at constant composition through changes in ionization alone – it is at such early-times that SNe II-P are best used for distance determinations based on spectroscopic modelling. Given the issues with the density structure, and the confinement of the photosphere to the outer layers at early times, it is clear that higher resolution pre-SN models are needed to allow more accurate results in our present modelling approach – specifically we require that the outer SN ejecta be resolved and accurately described all the way to large velocities.

(viii) At the same colour, photospheric spectra show excellent agreement with those of SN1999em. Nebular spectra, with the exception of the H I spectrum, are also strikingly similar to those observed. The problem with the H I lines is directly attributable to the neglect of excitation/ionization by non-thermal electrons. In our models only forbidden lines of O, Na, Ca, Ti and Fe, and resonance lines of Ca shine at a few 100 d after explosion (in the optical and/or near-IR ranges). At 1000 d after explosion, the spectra are dominated by the doublet line of O I and numerous lines of Fe I–II; no other species included in our calculations seems to contribute at such late times.

(ix) The s15e12 and s25e12 models show differences in peak luminosity and the rise-time to peak *V*-band brightness. However, at the same colour, photospheric spectra are very similar. This suggests that the composition contrast between the two progenitors is too small to be observable spectroscopically during the 'plateau' phase. It also corroborates the spectral degeneracy of SNe II-P spectra and highlights the difficulty of distinguishing between different progenitor masses or evolutionary paths based on 'plateau' phase spectra.

We find that nebular-phase spectra show differences that unambiguously distinguish a lower-mass progenitor from a higher-mass progenitor in a standard SN II-P explosion. These are related to the property that stars with higher main-sequence masses have systematically a higher helium-core mass, and shows up in late-time [O I] 6303–6363 Å line profiles, which appear broader and stronger for a higher-mass progenitor (Dessart et al. 2010a).

In this work, we have demonstrated that there is much to learn from synthetic spectra of SNe II-P. Spectra contain additional information that is either absent or degenerate in multi-band light curves alone. Ultimately, it is through non-LTE time-dependent radiative-transfer simulations of a large set of non-rotating and rotating pre-SN RSG stars, evolved at various metallicities, that an accurate mapping between SNe II-P observations and progenitor/explosions properties will be possible. We plan to undertake this task in the near future. Securing a large data set of photospheric- and nebular-phase observations of SNe II-P, covering all stages of temporal evolution, is essential for the fulfilment of this task.

Downloaded from https://academic.oup.com/mnras/article/410/3/1739/962985 by CNRS - ISTO user on 30 November 2021

ACKNOWLEDGMENTS

We thank Stan Woosley for providing the input hydrodynamical models that were used as initial conditions for our radiative-transfer calculations. LD acknowledges financial support from the European Community through an International Re-integration Grant, under grant number PIRG04-GA-2008-239184. LD also acknowledges financial support in the early stages of this work from the Scientific Discovery through Advanced Computing (SciDAC) program of the DOE, under grant number DOE-FC02-06ER41452. DJH acknowledges support from STScI theory grant HST-AR-11756.01.A and NASA theory grant NNX10AC80G.

REFERENCES

Ambwani K., Sutherland P., 1988, ApJ, 325, 820
Axelrod T. S., 1980, PhD thesis, California Univ., Santa Cruz
Baklanov P. V., Blinnikov S. I., Pavlyuk N. N., 2005, Astron. Lett., 31, 429
Baron E., Branch D., Hauschildt P. H., 2007, ApJ, 662, 1148
Bersten M. C., Hamuy M., 2009, ApJ, 701, 200
Blinnikov S., Lundqvist P., Bartunov O., Nomoto K., Iwamoto K., 2000, ApJ, 532, 1132
Burrows A., Dessart L., Livne E., Ott C. D., Murphy J., 2007a, ApJ, 664, 416
Burrows A., Livne E., Dessart L., Ott C. D., Murphy J., 2007b, ApJ, 655, 416
Cappellaro E., Turatto M., Tsvetkov D. Y., Bartunov O. S., Pollas C., Evans R., Hamuy M., 1997, A&A, 322, 431
Castor J. I., 1970, MNRAS, 149, 111
Chornock R., Filippenko A. V., Li W., Silverman J. M., 2010, ApJ, 713, 1363
Cohen M., Wheaton W. A., Megeath S. T., 2003, AJ, 126, 1090
Colgate S. A., White R. H., 1966, ApJ, 143, 626
Dessart L., Hillier D. J., 2005a, A&A, 439, 671
Dessart L., Hillier D. J., 2005b, A&A, 437, 667
Dessart L., Hillier D. J., 2006, A&A, 447, 691
Dessart L., Hillier D. J., 2008, MNRAS, 383, 57
Dessart L., Hillier D. J., 2009, in Giobbi G., Tornambe A., Raimondo G., Limongi M., Antonelli L. A., Menci N., Brocato E., eds, AIP Conf. Ser. Vol. 1111, Probing Stellar Populations out to the Distant Universe. Am. Inst. Phys., New York, p. 565
Dessart L., Hillier D. J., 2010, MNRAS, 405, 2141
Dessart L. et al., 2008, ApJ, 675, 644
Dessart L., Livne E., Waldman R., 2010a, MNRAS, 408, 827
Dessart L., Livne E., Waldman R., 2010b, MNRAS, 405, 2113
Eastman R. G., Woosley S. E., Weaver T. A., Pinto P. A., 1994, ApJ, 430, 300
Eastman R. G., Schmidt B. P., Kirshner R., 1996, ApJ, 466, 911
Falk S. W., Arnett W. D., 1977, ApJS, 33, 515
Gezari S. et al., 2008, ApJ, 683, L131
Hamuy M., 2003, ApJ, 582, 905
Hamuy M., Pinto P. A., 2002, ApJ, 566, L63
Hamuy M. et al., 2001, ApJ, 558, 615
Heger A., Fryer C. L., Woosley S. E., Langer N., Hartmann D. H., 2003, ApJ, 591, 288
Hillier D. J., Miller D. L., 1998, ApJ, 496, 407
Kasen D., Woosley S. E., 2009, ApJ, 703, 2205
Kasen D., Thomas R. C., Nugent P., 2006, ApJ, 651, 366
Kirshner R. P., Kwan J., 1974, ApJ, 193, 27
Kozma C., Fransson C., 1992, ApJ, 390, 602
Kozma C., Fransson C., 1998a, ApJ, 496, 946
Kozma C., Fransson C., 1998b, ApJ, 497, 431
Kurucz R. L., 2009, in Hubeny I., Stone J. M., MacGregor K., Werner K., eds, AIP Conf. Ser. Vol. 1171, Recent directions in astrophysical quantitative spectroscopy and radiation hydrodynamics. Am. Inst. Phys., New York, p. 43
Landolt A. U., 1992, AJ, 104, 340
Lançon A., Hauschildt P. H., Ladjal D., Mouhcine M., 2007, A&A, 468, 205
Leonard D. C., Filippenko A. V., 2005, in Turatto M., Benetti S., Zampieri L., Shea W., eds, ASP Conf. Ser. Vol. 342, Supernovae as Cosmological Lighthouses. Astron. Soc. Pac., San Francisco, p. 330
Leonard D. C. et al., 2002, PASP, 114, 35
Leonard D. C. et al., 2006, Nat, 440, 505
Levesque E. M., Massey P., Olsen K. A. G., Plez B., Josselin E., Maeder A., Meynet G., 2005, ApJ, 628, 973
Li H., McCray R., 1992, ApJ, 387, 309
Li H., McCray R., 1993, ApJ, 405, 730
Li H., McCray R., 1995, ApJ, 441, 821
Litvinova I. Y., Nadezhin D. K., 1985, Sov. Astron. Lett., 11, 145
Lucy L. B., 1991, ApJ, 383, 308
Marek A., Janka H., 2009, ApJ, 694, 664
Mazzali P. A., Lucy L. B., Butler K., 1992, A&A, 258, 399
McCray R., 1993, ARA&A, 31, 175
Meynet G., Maeder A., 2000, A&A, 361, 101
Meynet G., Ekström S., Maeder A., 2006, A&A, 447, 623
Mitchell R. C., Baron E., Branch D., Hauschildt P. H., Nugent P. E., Lundqvist P., Blinnikov S., Pun C. S. J., 2002, ApJ, 574, 293
Phillips M. M., Heathcote S. R., Hamuy M., Navarrete M., 1988, AJ, 95, 1087
Phillips M. M., Hamuy M., Heathcote S. R., Suntzeff N. B., Kirhakos S., 1990, AJ, 99, 1133
Poznanski D. et al., 2009, ApJ, 694, 1067
Rabinak I., Waxman E., 2010, preprint (arXiv e-prints)
Smartt S. J., 2009, ARA&A, 47, 63
Smartt S. J., Eldridge J. J., Crockett R. M., Maund J. R., 2009, MNRAS, 395, 1409
Sugerman B. E. K. et al., 2006, Sci, 313, 196
Swartz D. A., 1991, ApJ, 373, 604
Swartz D. A., Filippenko A. V., Nomoto K., Wheeler J. C., 1993, ApJ, 411, 313
Swartz D. A., Sutherland P. G., Harkness R. P., 1995, ApJ, 446, 766
Tominaga N., Blinnikov S., Baklanov P., Morokuma T., Nomoto K., Suzuki T., 2009, ApJ, 705, L10
Utrobin V. P., 2007, A&A, 461, 233
Utrobin V. P., Chugai N. N., 2005, A&A, 441, 271
Weaver T. A., Zimmerman G. B., Woosley S. E., 1978, ApJ, 225, 1021
Woosley S. E., Heger A., 2007, Phys. Rep., 442, 269
Woosley S. E., Weaver T. A., 1995, ApJS, 101, 181
Woosley S. E., Heger A., Weaver T. A., 2002, Rev. Modern Phys., 74, 1015
Xu Y., McCray R., 1991, ApJ, 375, 190
Xu Y., Ross R. R., McCray R., 1991, ApJ, 371, 280
Xu Y., McCray R., Oliva E., Randich S., 1992, ApJ, 386, 181

This paper has been typeset from a TEX/LATEX file prepared by the author.

Downloaded from https://academic.oup.com/mnras/article/410/3/1739/962985 by CNRS - ISTO user on 30 November 2021